

Analysis of pedestal plasma transport

To cite this article: J.D. Callen *et al* 2010 *Nucl. Fusion* **50** 064004

View the [article online](#) for updates and enhancements.

Related content

- [Comparing 1.5D ONETWO and 2D SOLPS analyses of inter-ELM H-mode plasma in DIII-D](#)
L.W. Owen, J.M. Canik, R.J. Groebner *et al.*
- [Chapter 2: Plasma confinement and transport](#)
E.J. Doyle (Chair Transport Physics), W.A. Houlberg (Chair Confinement Database and Modelling), Y. Kamada (Chair Pedestal and Edge) *et al.*
- [Review Article](#)
M Hirsch, J Baldzuhn, C Beidler *et al.*

Recent citations

- [Dynamics of the pedestal transport during edge localized mode cycles at ASDEX Upgrade](#)
E Viezzer *et al*
- [The role of edge resonant magnetic perturbations in edge-localized-mode suppression and density pump-out in low-collisionality DIII-D plasmas](#)
Q.M. Hu *et al*
- [Modeling the Edge-Plasma Interface for Liquid-Lithium Walls in FNSF](#)
M. E. Rensink *et al*



IOP | ebooks™

Bringing together innovative digital publishing with leading authors from the global scientific community.

Start exploring the collection—download the first chapter of every title for free.

Analysis of pedestal plasma transport

J.D. Callen¹, R.J. Groebner², T.H. Osborne², J.M. Canik³,
L.W. Owen³, A.Y. Pankin⁴, T. Rafiq⁴, T.D. Rognlien⁵ and
W.M. Stacey⁶

¹ Department of Engineering Physics, University of Wisconsin, Madison, WI 53706-1609, USA

² General Atomics, San Diego, CA 92186-5608, USA

³ Oak Ridge National Laboratory, Oak Ridge, TN 37831, USA

⁴ Department of Physics, Lehigh University, Bethlehem, PA 18015-3182, USA

⁵ Lawrence Livermore National Laboratory, Livermore, CA 94551-0808, USA

⁶ Georgia Tech, Atlanta, GA 30332, USA

E-mail: callen@engr.wisc.edu and groebner@fusion.gat.com

Received 19 October 2009, accepted for publication 12 May 2010

Published 28 May 2010

Online at stacks.iop.org/NF/50/064004

Abstract

An H-mode edge pedestal plasma transport benchmarking exercise was undertaken for a single DIII-D pedestal. Transport modelling codes used include 1.5D interpretive (ONETWO, GTEDGE), 1.5D predictive (ASTRA) and 2D ones (SOLPS, UEDGE). The particular DIII-D discharge considered is 98889, which has a typical low density pedestal. Profiles for the edge plasma are obtained from Thomson and charge-exchange recombination data averaged over the last 20% of the average 33.53 ms repetition time between type I edge localized modes. The modelled density of recycled neutrals is largest in the divertor X-point region and causes the edge plasma source rate to vary by a factor $\sim 10^2$ on the separatrix. Modelled poloidal variations in the densities and temperatures on flux surfaces are small on all flux surfaces up to within about 2.6 mm ($\rho_N > 0.99$) of the mid-plane separatrix. For the assumed Fick's-diffusion-type laws, the radial heat and density fluxes vary poloidally by factors of 2–3 in the pedestal region; they are largest on the outboard mid-plane where flux surfaces are compressed and local radial gradients are largest. Convective heat flows are found to be small fractions of the electron ($\lesssim 10\%$) and ion ($\lesssim 25\%$) heat flows in this pedestal. Appropriately averaging the transport fluxes yields interpretive 1.5D effective diffusivities that are smallest near the mid-point of the pedestal. Their 'transport barrier' minima are about 0.3 (electron heat), 0.15 (ion heat) and 0.035 (density) $\text{m}^2 \text{s}^{-1}$. Electron heat transport is found to be best characterized by electron-temperature-gradient-induced transport at the pedestal top and paleoclassical transport throughout the pedestal. The effective ion heat diffusivity in the pedestal has a different profile from the neoclassical prediction and may be smaller than it. The very small effective density diffusivity may be the result of an inward pinch flow nearly balancing a diffusive outward radial density flux. The inward ion pinch velocity and density diffusion coefficient are determined by a new interpretive analysis technique that uses information from the force balance (momentum conservation) equations; the paleoclassical transport model provides a plausible explanation of these new results. Finally, the measurements and additional modelling needed to facilitate better pedestal plasma transport modelling are discussed.

PACS numbers: 52.55.Fa, 52.25.Fi, 52.55.Dy, 52.55.Rk

(Some figures in this article are in colour only in the electronic version)

1. Introduction

Large edge pedestals in high- (H-) confinement mode plasmas are critical [1] for achieving high fusion power in ITER [2]. At present, plasma transport processes and their role in H-mode pedestals are not well understood. In this work we seek to identify, clarify and quantify the key transport processes involved in H-mode pedestals in the quasi-equilibrium transport state between type I edge localized modes (ELMs). Specifically, an H-mode edge pedestal (HEP) benchmarking exercise (BE) for a single DIII-D pedestal has

been undertaken in which transport modelling results from various types of modelling codes are extensively compared and benchmarked for a single, well-characterized, typical H-mode pedestal in the DIII-D tokamak [3]. The initial objectives of the HEP BE were to (1) determine channels of energy flow through and losses from the pedestal; (2) identify key physical processes for characterizing these energy flows to (a) determine what key experimental measurements are most needed, (b) clarify what processes need to be included in transport modelling and (c) increase confidence in transport modelling as various code results converge and (3) facilitate

meaningful, reliable comparisons with theory-based transport models.

Transport analyses are most straightforward when plasmas are in transport equilibrium. But H-mode pedestals evolve [4] between ELMs. There is a wide variability in the time scales for edge pedestals to re-build between ELMs. However, in an exploration [4] of pedestals after type I ELMs in DIII-D that were slowly evolving, it was shown that after an ELM the average pedestal pressure gradient first increased ‘rapidly’ on a time scale of about 10–20 ms to a ‘transport quasi-equilibrium;’ it then increased more slowly for ~30–100 ms, until the next ELM. An ~10 ms transient phase is consistent with the time scale for diffusive transport over a thin pedestal width $\Delta x \sim 0.03$ m for $D \sim 0.1$ m² s⁻¹: $\tau \sim (\Delta x)^2/D \sim 9$ ms.

In this study we analyse plasma transport properties in the transport quasi-equilibrium phase just before the next ELM. The particular pedestal considered is from a typical low pedestal density DIII-D discharge. It will be characterized by data obtained by averaging over the last 20% of the average 33.53 ms period between type I ELMs from about 4 to 5 s in DIII-D discharge 98889. Plasma transport properties will be analysed mainly from the core region inside the top of the pedestal (from normalized radius $\rho_N \simeq 0.85$) through the pedestal ($0.94 \lesssim \rho_N \leq 1.0$) out to the separatrix ($\rho_N = 1$).

To explore the role and importance of the many diverse properties of plasma sources, sinks and transport involved in the pedestal, a number of different types of transport codes will be used. The particular codes involved are the 1.5D (one-dimensional (1D) ‘radial’ transport across shaped flux surfaces) core-based interpretive transport code often used to analyse DIII-D plasmas (ONETWO [5]), a 1.5D pedestal-focused interpretive transport code (GTEDGE [6]), a 1.5D predictive transport code (ASTRA [7]) and two-dimensional (2D) edge-divertor region codes (SOLPS [8], UEDGE [9, 10]) run in interpretive and semi-predictive modes. A key contribution of these codes is that they quantify the various sources (e.g. heating by energetic neutral beams, fuelling by recycling neutrals) and sinks (e.g. radiative energy losses) of density, momentum and energy in the plasma. This information allows one to determine via ‘interpretive’ transport analysis the plasma transport required to obtain the experimentally measured density and temperature profiles. Conversely, in ‘predictive’ transport analysis one uses theoretically predicted plasma transport properties to predict the profiles.

The 1.5D codes are applicable for closed, nested flux surfaces inside a divertor separatrix and take account of the non-circular plasma cross-section. They average over the flux surfaces to obtain a 1D description of plasma sources and sinks and plasma density and energy transport ‘radially’ across toroidal magnetic flux surfaces. The ONETWO and ASTRA codes have been extensively benchmarked against lots of core plasma data and carefully account for plasma sources and sinks in the core plasma. They use a combination of collisional (neoclassical) and (in predictive modes) various analytic-based anomalous plasma transport models. Since the ONETWO code is used to analyse plasma transport in many DIII-D discharges, its results will generally be the ‘reference’ against which other code results will be compared. The GTEDGE

code concentrates on the pedestal region using a 1.5D transport model interfaced with results from a 2D kinetic-based neutral source model; it includes consideration of momentum (force balance) equations for each plasma species. The 2D codes (SOLPS, UEDGE) have traditionally focused on modelling divertor plasma properties outside the separatrix. They allow for and determine poloidal variations in plasma sources, sinks and properties. The 2D codes use local poloidal-magnetic-flux-surface-based coordinates that are applicable both inside and outside the separatrix. They determine plasma properties all the way from the core plasma through the pedestal region and scrape-off layer outside the separatrix, out to vacuum wall and divertor plate boundaries where plasma–wall interactions occur and are included. The 2D codes use the Braginskii [11] collisional plasma transport model with ad hoc additions of anomalous radial plasma particle and energy diffusivities. The SOLPS code uses a Monte Carlo-based kinetic neutral model while the UEDGE code uses a fluid neutrals model. A major issue that will be addressed in this paper (mainly in section 7) is, how far out radially (in the pedestal, towards the separatrix) can 1.5D codes capture the most important transport processes and where do which 2D processes become important in the pedestal?

This paper is organized as follows. The next section describes the particular DIII-D discharge 98889 being considered and its pedestal plasma properties. The following section describes the transport modelling procedures used by the various codes; mathematical details of the coordinate systems they use are discussed in the appendix. Section 4 presents the effective diffusivity coefficients for electron and ion heat in this pedestal obtained via interpretive modelling. Comparisons of these effective heat diffusivity coefficients with various analytic-based theoretical predictions are discussed in the following section. The next section describes ASTRA predictive modelling of the pedestal electron temperature profile. Pedestal plasma transport analyses from the 2D codes are discussed in section 7 which emphasizes the poloidal asymmetry of the recycling neutrals fuelling source and discusses the degree to which 1.5D codes capture the needed physics inside the separatrix. The 1.5D density transport analysis is discussed in section 8. The next section discusses the new interpretive procedure for determining the density pinch and a possible explanation of it. Section 10 discusses some of the largest uncertainties in the present plasma transport analyses. It also discusses the experimental measurements and modelling extensions most needed to resolve these uncertainties and facilitate better modelling of pedestal plasma transport properties. The final section summarizes the present conclusions of this HEP BE study.

2. Experimental characterization of DIII-D H-mode pedestal

The pedestal to be studied comes from DIII-D discharge 98889, which has been well characterized. Waveforms for various key plasma parameters in this lower single null (LSN) divertor discharge during the time over which averaged profiles are obtained are shown in figure 1. As can be ascertained from this figure, during this time window the ELMs are relatively reproducible; the average time between ELMs is

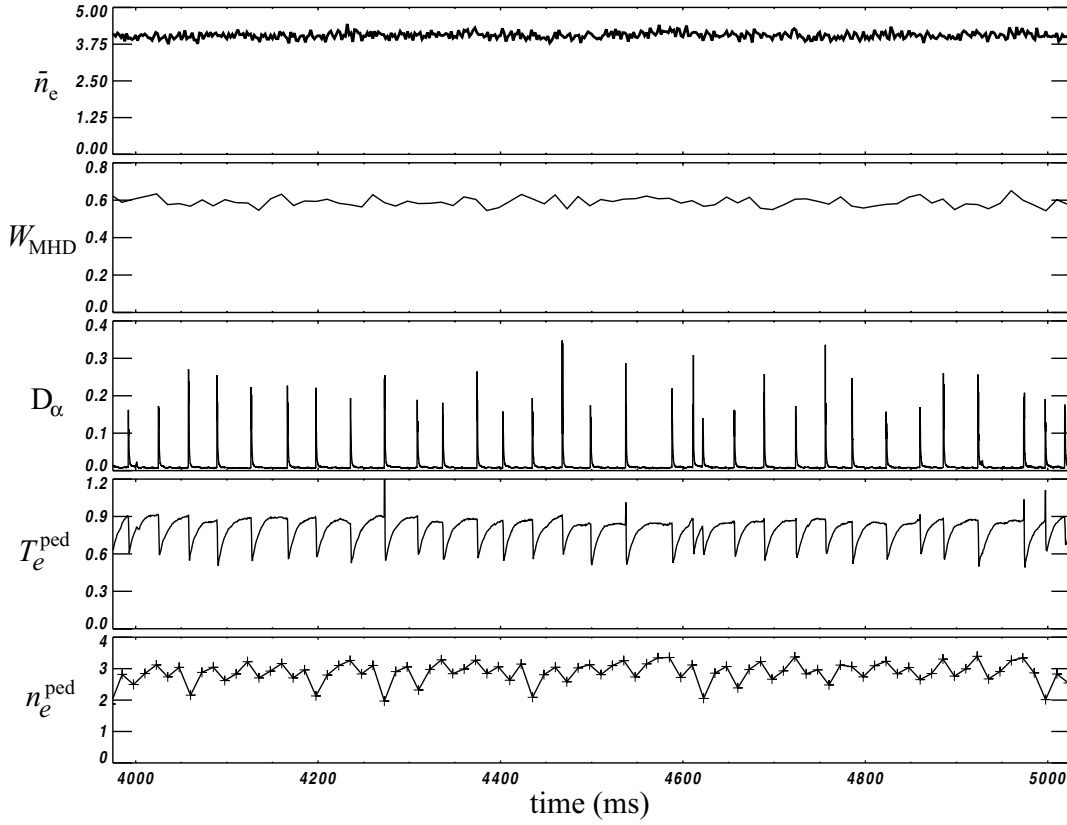


Figure 1. Waveforms for line-averaged electron density $\bar{n}_e/(10^{19} \text{ m}^{-3})$, plasma stored energy W_{MHD} (MJ), deuterium Balmer alpha (D_α) emission, electron temperature T_e^{ped} (keV) at the top of pedestal measured by ECE and electron density $n_e^{\text{ped}}/(10^{19} \text{ m}^{-3})$ at the top of the pedestal at the times of the TS measurements, in DIII-D discharge 98889.

33.53 ms; and the pedestal electron temperature recovers to its transport quasi-equilibrium value in about 10 ms. Microwave reflectometry data have recently become available on DIII-D. It shows the density pedestal in discharges similar to 98889 recover on a similar time scale—see figure 9 in [12]. The Thomson scattering (TS) data in the bottom trace of figure 1 is consistent with such a recovery time, but too widely spaced in time to be definitive.

In order to reduce scatter in the TS data and facilitate referencing these data to the separatrix, an averaging procedure was used to obtain composite quasi-equilibrium plasma profiles. The averaging procedure was enabled by the fact that the ELMs were relatively reproducible (see figure 1) over the 4 to 5 s time window used. First, pedestal region magnetic flux surfaces were obtained by solving the Grad–Shafranov equation using the EFIT free boundary code [13] for each Thomson time in figure 1 allowing for a finite current on the separatrix and using the usual magnetic diagnostics to constrain the EFIT solutions. Previous analyses in DIII-D have identified [14] that the best measure of the separatrix location is where the electron temperature is about 100 eV, as determined by the transition to open field lines outside the separatrix. Also, it was shown [14, 15] that the pedestal profiles can be best fit by hyperbolic tangent (tanh) fitting functions. Thus, next a nonlinear least squares fitter was used to obtain a tanh fit for the Thomson data in 20% windows of the ELM cycles. Then, the Thomson profile flux coordinate positions were adjusted so the tanh fit T_e on the separatrix is a common, physics-determined

value, in this case 90 eV. Further details on the fitting procedure and its uncertainties are provided in section 2 of [16].

The resultant composite plasma profiles are then used to develop full ‘kinetic’ EFIT equilibria at a few specific times during the average ELM cycle. These equilibria contain the best available reconstructions of the pressure and current density profiles. An example of flux surfaces from a kinetic EFIT is shown in figure 2. This equilibrium represents the 60–80% interval of the average ELM cycle and is labelled with a time of 4523 ms, which is 70% of an average ELM period after the mid-point of the 4 to 5 s averaging time interval. The cross-section of the flux surfaces is shown along with the corresponding cylindricalized (see next section and the appendix) flux surface of the separatrix. The toroidal magnetic field at the geometric centre of the vacuum vessel at $R_0 = 1.6955 \text{ m}$ is $B_{t0} = 2 \text{ T}$. For this magnetic equilibrium the magnetic axis is at $R_m \simeq 1.75 \text{ m}$. The mid-plane half radius r_M is $\simeq 0.6 \text{ m}$. However, the average radius, which is defined in terms of the toroidal magnetic flux Φ at the separatrix by $a \equiv \sqrt{\Phi(\text{sep})/\pi B_{t0}}$, is 0.7667 m . It is larger than r_M because the plasma has an edge ellipticity of $\kappa = 1.76$ and a triangularity of $\delta = -0.02$. Other parameters during the near steady-state conditions to be analysed are plasma current $I = 1.22 \text{ MA}$ and $q_{95} \simeq 4.44$.

Interpretive modelling with ONETWO indicates the total input power was 3.21 MW, from a combination of energetic neutral beams (2.91 MW of which 1.17 MW goes to electrons, 1.74 MW to ions) and ohmic heating (0.3 MW). This total input

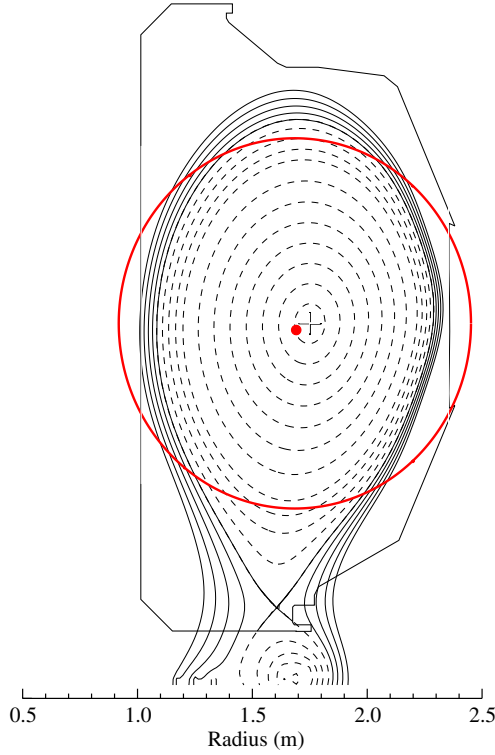


Figure 2. EFIT magnetic flux surfaces are nested about the magnetic axis at $R_m \simeq 1.75$ m and $Z = 0$ in the analysed DIII-D discharge 98889. Also shown is the cylindricalized radius $a \simeq 0.7667$ m of the separatrix magnetic flux surface which is centred at $R_0 \simeq 1.683$ m and $Z \simeq -0.035$ m. The region ($0.85 \leq \rho_N \leq 1.0$) whose plasma transport properties are analysed in this work lies between the third from last dashed flux surface and the magnetic separatrix. The pedestal region $0.95 \leq \rho_N \leq 1.0$ lies between the last dashed flux surface and the separatrix.

power is about a factor of 4 higher than the L–H transition power threshold of 0.75 MW determined from the latest ITER scaling [17] at an earlier time when the density is lower. Global plasma parameters are as follows: central electron temperature $T_e(0) = 3.2$ keV and deuterium ion temperature $T_i(0) = 4.6$ keV, toroidal beta $\beta_t = 0.013$, poloidal beta $\beta_p = 0.59$, thermal energy confinement time $\tau_E \simeq 0.153$ s [$H_{\text{ITER98y2}} \simeq 1.02$] and estimated particle confinement time $\tau_p \simeq 0.4$ s.

The composite profiles of the electron density and temperature, and ion temperature are shown in figure 3. Data for the electron density n_e and temperature T_e were obtained from a multi-point, multi-time TS system [18], which has a high density of viewing chords in the pedestal region. The edge channels view along the vertical Thomson laser; they are separated by 1.3 cm (about 0.013 in ρ_N) with the spot size being comparable to the separation. Thomson profile measurements were made every 12–13 ms throughout the discharge considered here. Data for the ion temperature T_i were obtained from a charge-exchange recombination (CER) spectroscopy system, which views the C VI 5290.5 Å line [19]. This system also has a high density of view chords in the pedestal region with a separation of tangential chords, oriented along the outer mid-plane, of about 0.6 cm (about 0.01 in ρ_N) and a spot size slightly smaller than the chord separation. A system of vertically viewing chords is interleaved with the edge

chords and is often used to improve the spatial resolution for T_i . The T_i data were acquired with an averaging time of 10 ms. The TS tanh fits at the separatrix ($\rho_N = 1$) yield $n_e(1) \simeq 0.077 \times 10^{20} \text{ m}^{-3}$ and $T_e(1) \simeq 0.09$ keV. At the ρ_N symmetry points of the tanh fits $n_e(0.982) \simeq 0.165 \times 10^{20} \text{ m}^{-3}$ and $T_e(0.978) \simeq 0.39$ keV. Spline fits to the CER-determined ion temperature profiles were used in the various modelling codes, which yield $T_i(1) \simeq 0.28$ keV and $T_i(0.982) \simeq 0.49$ keV.

In figure 3 and throughout the rest of this paper we identify three key regions (I, II, III) of the edge plasma being analysed. There is no unique definition for the position of the ‘top’ of the pedestal. Here, we will define it to occur at $\rho_N \simeq 0.94$, which is about twice the width of region III in from the tanh symmetry points. Region III is defined to be from the symmetry points ($\rho_N \simeq 0.98$) of the pedestal tanh fits to the separatrix. Thus, region I will be the extension of the core plasma region out to the top of the pedestal, i.e. here $0.85 < \rho_N < 0.94$. Region II will be called the ‘top half’ of the pedestal and is defined by $0.94 < \rho_N < 0.98$. Finally, region III will be called the ‘bottom half’ of the pedestal and is defined by $0.98 < \rho_N < 1.0$.

3. Transport modelling equations and procedures

The fundamental plasma transport equations solved by all the codes used in this study are developed from the collisional Braginskii [11] density and energy equations for each species of charged particles in the plasma, which will be written initially in the form

$$\text{density : } \partial n / \partial t + \nabla \cdot n \mathbf{V} = S_n, \quad (1)$$

$$\text{energy : } \frac{\partial}{\partial t} \left(\frac{3}{2} n T \right) + \nabla \cdot \left(\mathbf{q} + \frac{5}{2} n T \mathbf{V} \right) = Q. \quad (2)$$

Here, n is the density (units of m^{-3}), \mathbf{V} is the flow velocity (m s^{-1}) and T is the temperature (eV) of the species being considered. The density source S_n ($\text{m}^{-3} \text{ s}^{-1}$) has been added to the usual Braginskii density equation to allow for particle sources and sinks. It is predominantly due to ionization of recycling thermal neutrals emanating from the LSN divertor X-point region in DIII-D discharge 98889—see section 7. (The net beam source of ions from ionization minus charge exchange of beam neutrals is only 10% of the recycling neutrals ionization source at $\rho_N = 0.85$ and is negligible in the pedestal region $0.94 \leq \rho_N \leq 1.0$.) The GTEDGE code [6] solves in addition various components of the species momentum (force balance) equation for the flow velocity components; these solutions and their consequences will be discussed in section 9.

In the energy equation, $(3/2)nT$ is the internal energy (eV m^{-3}), \mathbf{q} is the conductive heat flux (W m^{-2}) and $(5/2)nT\mathbf{V}$ is the convective heat flux (W m^{-2}). The Q (W m^{-3}) on the right side of the energy equation represents the net energy input to or loss from the species due to cross-species collisional energy exchange, Joule heating and energy sources and sinks; it will be discussed in the following paragraph. In ONETWO [5] and SOLPS [8] the ion flow energy $(1/2)m_i n_i |\mathbf{V}_i|^2$ is added to the ion internal energy and convective heat transport; this flow energy will be neglected because it gives only a very small modification ($\lesssim 1\%$) to the internal energy in the 98889 pedestal.

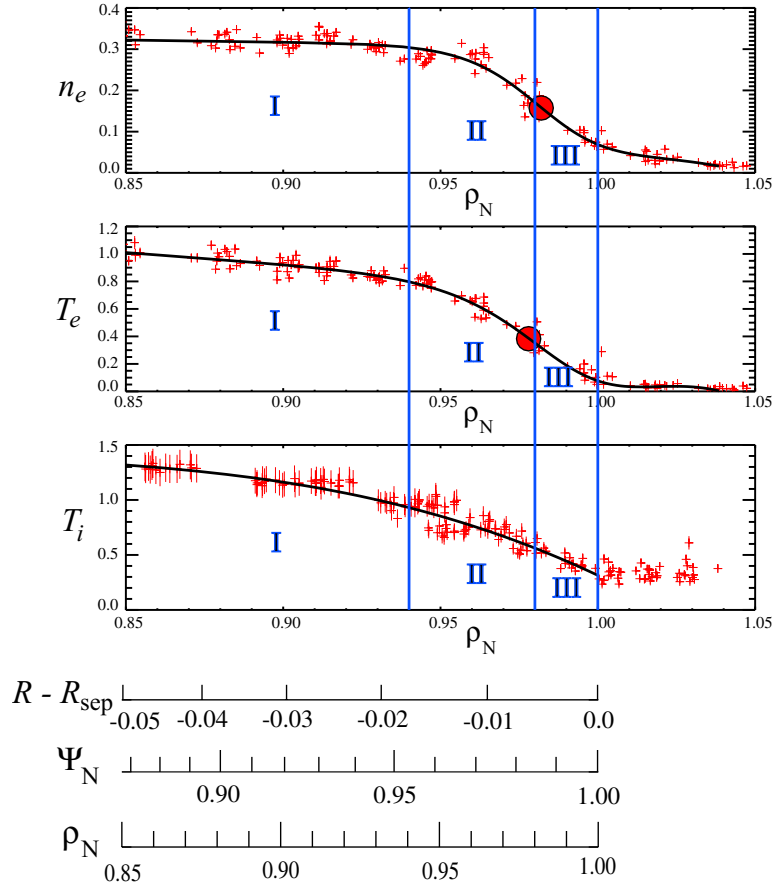


Figure 3. Edge profiles of (a) electron density $n_e/(10^{20} \text{ m}^{-3})$, (b) electron temperature $T_e(\text{keV})$ and (c) ion temperature $T_i(\text{keV})$. The fundamental normalized radial coordinate used here, $\rho_N \equiv \sqrt{\Phi/\pi B_0}/a$, is based on the toroidal magnetic flux Φ . Data used in obtaining the tanh fits (solid lines) are indicated by plus (+) symbols, which illustrate the degree of uncertainty in these profiles and the tanh function fits to them for n_e and T_e . The tanh ρ_N symmetry points are indicated by large dots (●) on the tanh fit lines. A spline fit is used for the T_i profile. The edge regions identified here are I core, II top and III bottom halves of the pedestal. The normalized poloidal flux coordinate Ψ_N and radial distance along the horizontal outboard mid-plane $R - R_{\text{sep}}$ (m) are indicated in rulers at the bottom.

The pedestal heating (or energy loss) rates per unit volume (power density) Q of electrons and ions have many components. The dominant ones from 1.5D ONETWO modelling are shown in figure 4. In the pedestal region $0.94 \leq \rho_N \leq 1$ (II and III), figure 4(a) shows that electrons are heated modestly by the collisional energy exchange Q_Δ (because $T_i > T_e$ in the pedestal), with smaller contributions due to Joule heating Q_{OH} and (nearly negligible) neutral beam heating $Q_{\text{e beam}}$. Radiative losses Q_{rad} are a significant but not dominant electron heat loss process in the pedestal. The radiated power is measured by a multi-chord, multi-channel bolometer array; the total radiated power is only 0.2 MW, predominantly due to carbon. (Electron impact ionization energy losses are $\lesssim 0.13 \times 10^4 \text{ W m}^{-3}$ in the pedestal and hence negligible.)

The dominant ion energy losses in the pedestal region $0.94 \leq \rho_N \leq 1$ (II and III) are more significant. They can be seen from figure 4(b) to be mainly due to charge-exchange and collisional energy transfer Q_Δ to the colder electrons. There is modest heating from the production of ions via electron impact ionization of recycling neutrals Q_{ion} .

Similar dominant contributions have been found in modelling of other DIII-D pedestals [20–23]. However, electron heating by neutral beams can be larger when the beam

power and pedestal density are higher [20–22]. There can also be larger charge-exchange ion energy losses when the ion temperature is higher near the separatrix [22].

Because the various transport modelling codes focus on different regions of the plasma, they use different coordinate systems. All the codes assume axisymmetry in the toroidal (angle ζ) direction. The 1.5D core transport codes (ONETWO, ASTRA) use magnetic flux coordinates based on the nested toroidal magnetic flux surfaces (toroidal flux $\psi_t \rightarrow \Phi$ in ONETWO, ASTRA). For their radial coordinate they use $\rho \equiv (\psi_t/\pi B_{t0})^{1/2}$, which is the average radius of the ψ_t or Φ toroidal flux surface. In this definition B_{t0} is the magnitude of the toroidal magnetic field at the geometric axis of the vacuum vessel (i.e. at $R_0 = 1.6955 \text{ m}$). The core transport codes base their coordinate system on the toroidal magnetic flux because [24] during typical magnetic field transients (e.g. due to a non-inductive current drive being turned on) the toroidal magnetic field (flux ψ_t) changes (in magnitude and spatial structure) much less than the poloidal magnetic field (flux ψ_p), which is determined by the toroidal current distribution in the plasma. However, the toroidal flux ψ_t or Φ is not well defined outside the separatrix—because the area involved in its definition extends vertically through the vacuum vessel coils, past the divertor coils and vertically to infinity.

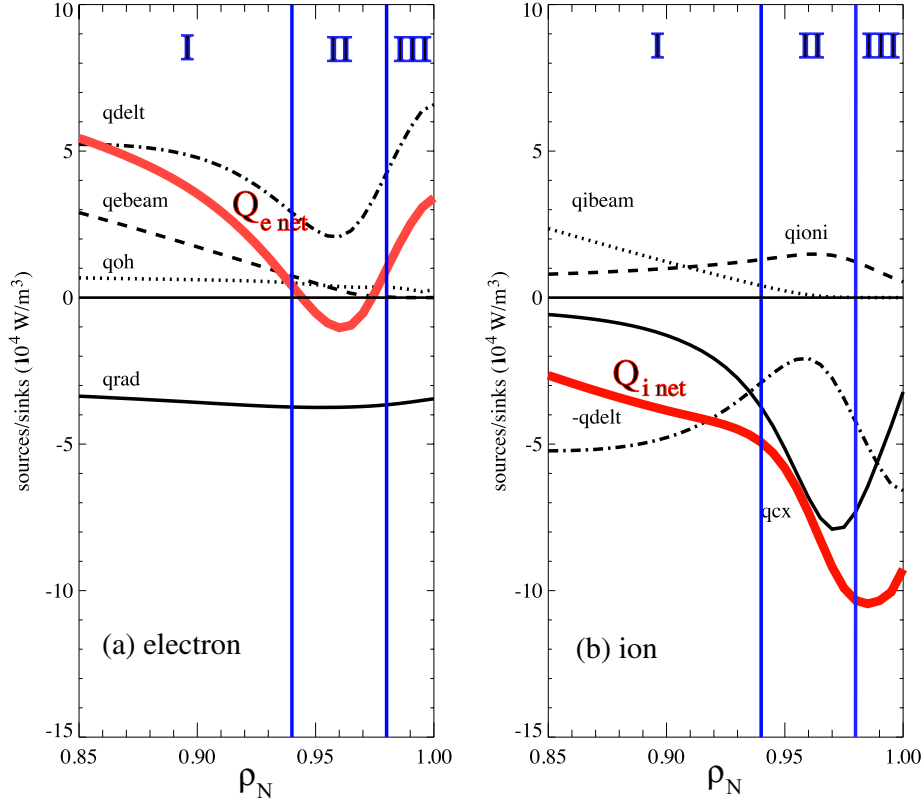


Figure 4. Dominant components of net heating per unit volume ($\times 10^4 \text{ W m}^{-3}$) in the 98889 edge plasma from ONETWO modelling: (a) net electron power density $Q_{e \text{ net}}$ due to cross-species collisional energy exchange Q_{Δ} (qdelt), neutral beam heating $Q_{e \text{ beam}}$ (qebeam), Joule heating Q_{OH} (qoh) and radiative losses Q_{rad} (qrad) and (b) net ion power density $Q_{i \text{ net}}$ due to cross-species collisional energy exchange $-Q_{\Delta}$ (-qdelt), neutral beam heating $Q_{i \text{ beam}}$ (qibeam), ionization minus recombination $Q_{i \text{ ion}}$ (qioni), and charge-exchange Q_{cx} (qcex).

The 2D codes (SOLPS and UEDGE), which focus on edge plasmas up to the divertor plate and the wall boundaries, use a poloidal-flux-based radial coordinate, which is well defined all the way to the divertor plates. In ONETWO the poloidal flux $\psi_p \rightarrow \Psi$ and a corresponding normalized radial coordinate $\Psi_N \equiv \Psi/\Psi_{\text{sep}}$ are often used. Both the toroidal and poloidal flux coordinates are applicable in the pedestal region in the quasi-equilibrium transport situation being studied here. The 2D codes often present results in terms of the radial distance from the separatrix on the horizontal mid-plane of the plasma cross-section, $R - R_{\text{sep}}$.

The rulers at the bottom of figure 3 show the relations between these three different radial coordinate systems in the plasma edge. This paper will present results primarily in terms of the normalized toroidal-flux-based radial coordinate $\rho_N \equiv \rho/a$, in which ρ is the average minor radius of the flux surface and $a \equiv (\psi_{t \text{ sep}}/\pi B_{t0})^{1/2}$ is the average minor radius of the separatrix (see figure 2).

We will be mainly interested in net plasma transport radially from one flux surface to the next. Thus, it is convenient to define the flux-surface average (FSA) of an axisymmetric (i.e. $\partial f/\partial \zeta = 0$, in which ζ is the toroidal angle) scalar function $f(x_\psi, x_\theta)$:

$$\langle f \rangle \equiv \lim_{\delta x_\psi \rightarrow 0} \frac{\int_{x_\psi}^{x_\psi + \delta x_\psi} d^3 x f}{\int_{x_\psi}^{x_\psi + \delta x_\psi} d^3 x} = \frac{2\pi \oint dx_\theta \sqrt{g} f}{dV/dx_\psi}. \quad (3)$$

Here, as discussed in the appendix, x_ψ is a generic radial flux-surface-based coordinate and x_θ is a generic poloidal

coordinate on a flux surface. Also, $\sqrt{g} \equiv 1/(\nabla x_\psi \cdot \nabla x_\theta \times \nabla \zeta) = (d\psi_p/dx_\psi)/B \cdot \nabla x_\theta$ is the Jacobian of the transformation from the laboratory to generic $(x_\psi, x_\theta, \zeta)$ flux-surface-based coordinates and $\oint dx_\theta$ indicates integration over the cyclic generic poloidal coordinate x_θ on a x_ψ flux surface. Also,

$$dV/dx_\psi \equiv V' = 2\pi \oint dx_\theta \sqrt{g} \quad (4)$$

is the radial derivative of the volume $V(x_\psi) \equiv \int_0^{x_\psi} d^3 x$ encompassed by the flux surface labelled by x_ψ . Note that V' has units of volume (m^3) divided by the units of x_ψ . The FSA of the divergence of a vector such as the particle flux Γ is

$$\langle \nabla \cdot \Gamma \rangle \equiv \frac{\partial}{\partial V} \langle \Gamma \cdot \nabla V \rangle = \frac{1}{V'} \frac{\partial}{\partial x_\psi} (V' \langle \Gamma \cdot \nabla x_\psi \rangle). \quad (5)$$

The FSA annihilates the poloidal (x_θ) derivative terms implicit in (1), (2) which are specified in (A.3), (A.4). Thus, the FSA density and energy equations become

$$\frac{\partial \langle n \rangle}{\partial t} + \frac{1}{V'} \frac{\partial}{\partial x_\psi} (V' \langle \Gamma \cdot \nabla x_\psi \rangle) = \langle S_n \rangle, \quad (6)$$

$$\frac{\partial}{\partial t} \left(\frac{3}{2} \langle nT \rangle \right) + \frac{1}{V'} \frac{\partial}{\partial x_\psi} \left(V' \left\langle \left(q + \frac{5}{2} T \Gamma \right) \cdot \nabla x_\psi \right\rangle \right) = \langle Q \rangle. \quad (7)$$

These are the 1D transport equations solved in the 1.5D modelling codes.

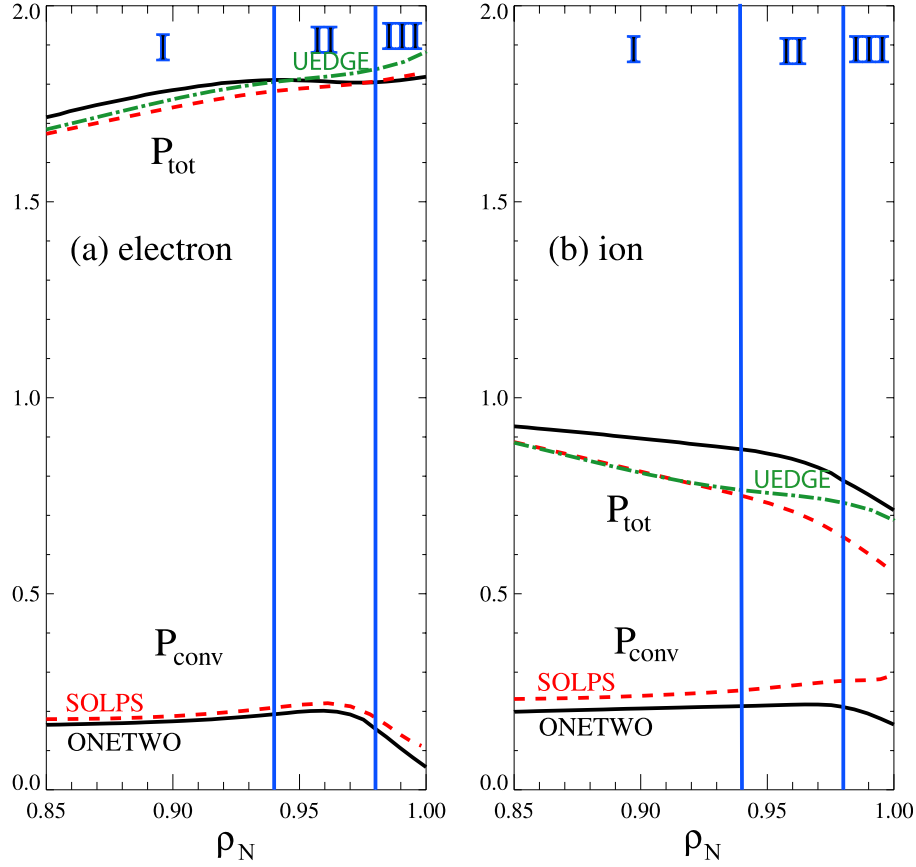


Figure 5. Heat flows through pedestal flux surfaces obtained from various modelling codes: (a) electron total and convective heat flows (MW) and (b) ion total and convective heat flows (MW).

4. Interpretive 1.5D modelling of heat transport

In general the radial fluxes Γ and q vary poloidally on a flux surface. However, in the core- and pedestal-relevant low (banana–plateau) collisionality regime where collision lengths are long compared with the poloidal periodicity length along magnetic field lines, net radial (i.e. across field lines) plasma transport from one flux surface to the next is the only physically meaningful quantity. In terms of the generic coordinates, the flow of a vector particle flux Γ across a flux surface is defined by $\int dS(x_\psi) \cdot \Gamma \equiv 2\pi \oint dx_\theta \sqrt{g} \Gamma \cdot \nabla x_\psi = (dV/dx_\psi) \langle \Gamma \cdot \nabla x_\psi \rangle = S(x_\psi) \langle \Gamma \cdot \nabla x_\psi \rangle / \langle |\nabla x_\psi| \rangle$. In obtaining the last forms we used $dS(x_\psi) \equiv 2\pi \sqrt{g} dx_\theta \nabla x_\psi = 2\pi \sqrt{g} dx_\theta |\nabla x_\psi| \hat{e}_{x_\psi}$, which can be used to show that the area of a flux surface is $S(x_\psi) = \langle |\nabla x_\psi| \rangle dV/dx_\psi$. Thus, the physically relevant net particle flow and electron and ion conductive heat flows (energy flowing) across a flux surface are

$$\dot{N}(x_\psi) \equiv \int dS(x_\psi) \cdot \Gamma = V' \langle \Gamma \cdot \nabla x_\psi \rangle, \quad s^{-1}, \quad (8)$$

$$P_{\text{cond}}(x_\psi) \equiv \int dS(x_\psi) \cdot q = V' \langle q \cdot \nabla x_\psi \rangle, \quad W. \quad (9)$$

As a check that all the modelling codes are beginning with the same ‘input data,’ in figure 5 we show the heat flows defined in (9) for the edge region. Here, the convective heat flow is defined by $P_{\text{conv}} \equiv \int dS(x_\psi) \cdot (5/2)nTV = V' \langle (5/2)T \Gamma \cdot \nabla x_\psi \rangle$. (The 5/2 factor in the convective heat

flow will be used throughout this paper since it arises naturally in the collisional Braginskii [11] fluid moment equations and is what most of these modelling codes usually use.) The conductive power P_{cond} will be defined as the total power flow P_{tot} minus the convective heat flow P_{conv} through the surface: $P_{\text{cond}} \equiv P_{\text{tot}} - P_{\text{conv}}$. It is an experimentally inferred quantity; i.e. it does not result from or necessarily imply the Fourier heat flux form (see equation (11) below) used below in interpretive analyses.

As can be seen in figure 5, the various modelling codes agree reasonably well on the heat flows through the pedestal region. The total electron power flow (~ 1.8 MW) through the pedestal is nearly constant with ρ_N —because the net electron heating in this region (II and III) is rather small (see figure 4(a)). The total ion power flow (~ 0.7 MW) through the pedestal decreases somewhat with increasing ρ_N because of collisional energy losses to the colder electrons and charge-exchange losses there (see figure 4(b)). The net ion cooling power in the pedestal region (II and III, i.e. $0.94 \leq \rho_n \leq 1$), which has a volume $\delta V \simeq 1.5 \text{ m}^3$, is $\delta P_i \simeq \delta V Q_i \sim (1.5 \text{ m}^3)(-10^5 \text{ W m}^{-3}) \sim -0.15 \text{ MW}$. Since variations in heat flows through the pedestal region are relatively small fractions of net energy flows there, the energy balances in this pedestal are dominated by the heat flows through the pedestal region, not by local heating or cooling processes there. However, the ion cooling processes are significant in the pedestal and become progressively more important as one approaches the separatrix (cf figure 5(b)). Previous transport analyses [20–22]

of radial heat flows in similar DIII-D pedestals have come to similar conclusions, except for cases where larger charge-exchange ion heat losses near the separatrix strongly reduce the conductive ion heat flow [20, 21].

Figure 5 also shows that the convective heat flow is relatively small for the pedestal we are considering; it is largest near the separatrix where it is about 10% of the total electron heat flow and about 25% of the total ion heat flow. The variability in the modelling code results for convective heat flows near the separatrix is caused mainly by differences in models of the plasma fuelling by recycling thermal neutrals. Section 7 will discuss the neutral models used in the various codes; in particular, the 2D neutral models and their effects on the particle flow \dot{N} defined in (8) are discussed there. The density transport properties in the pedestal are discussed in sections 8 and 9.

Plasma transport (caused by collisions and microturbulence) is often characterized by effective diffusivity coefficients for particle and heat transport. Specifically, in analogy with the kinetic theory of gases, one assumes the particle flux is given by a Fick's diffusion law $\Gamma = -D\nabla n$ and the conductive heat fluxes are in the Fourier heat flux form $q = -n\chi\nabla T$. The effective diffusion coefficients D and χ , which have units of $\text{m}^2 \text{s}^{-1}$, are determined 'interpretively' from experimental data by dividing the transport fluxes by the appropriate plasma gradients. While this procedure neglects possible 'off-diagonal' transport fluxes (e.g. particle fluxes induced by temperature gradients) and possible 'pinch' flux (or threshold gradient) effects, it does provide a measure of the transport required by a dominantly diffusive process to yield a given transport flux in response to the respective plasma gradient. Plausible pinch flow effects in density transport will be discussed in sections 8 and 9.

Plasmas in the hot core of tokamaks often hover near the threshold for the onset of drift-wave-type microinstabilities. Then, small changes in temperature or density gradients can cause very large changes in transport fluxes. For such cases the recommended procedure [25] for analysing plasma transport is to use theoretical or computational predictions of the (highly nonlinear) transport fluxes Γ and q in equations (6) and (7) to determine the density and temperature profiles. Unfortunately, this procedure is not useful here, mainly because, as discussed in sections 5 and 6, most drift-wave-type modes are stable and/or cause little or no radial plasma transport in the pedestal region, especially in its bottom half (III). Recently, MHD-like kinetic ballooning modes (KBMs) have been advanced [26] as a similar possible determiner of the pedestal pressure profile gradient; however, the nonlinear evolution (turbulence or intermittency?) of KBMs and possible transport representation of their effects have not yet been developed. Here, we will use the original, more primitive procedure of interpreting effective heat and particle diffusivities from the ratio of transport fluxes to plasma gradients, which gives at least an initial perspective on the relative amounts of plasma transport taking place in the various electron and ion density and heat transport channels.

Further assumptions are needed to facilitate comparisons of radial transport in 1.5D and 2D codes. First, one usually assumes the plasma density and temperatures are approximately constant on flux surfaces; section 7 will show that this is the case for the 98889 DIII-D pedestal.

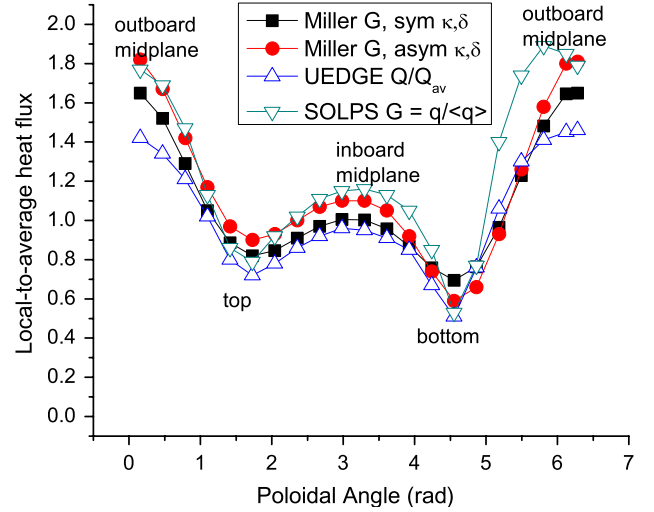


Figure 6. Poloidal variation of radial electron heat flux ($\propto |\nabla \rho|$) at the edge of the core plasma for χ_e constant on a flux surface: from UEDGE and SOLPS modelling and from estimates of $|\nabla \rho|$ (dots, squares) using the analytic Miller geometry model [27]. (Reprinted from [28]. Copyright © 2008 American Institute of Physics.)

Next, the diffusivities are assumed to be constant on flux surfaces. Physically, diffusivities and transport fluxes vary significantly on flux surfaces; they usually peak strongly on the tokamak's outboard side where particle gyroradii and drift orbit excursions from flux surfaces are largest and microinstabilities 'balloon.' However, characterizing radial transport by diffusion coefficients that are constant on flux surfaces is reasonable in the low collisional regimes of interest here where the collision lengths exceed the poloidal periodicity length which causes the only relevant transport to be from one magnetic flux surface to the next. Thus, labelling flux surfaces for simplicity as in the ONETWO and ASTRA codes by $x_\psi \rightarrow \rho$, the Fick's diffusion and Fourier heat flux laws become

$$\Gamma = -D(\rho)\nabla n = -D\nabla \rho \, dn/d\rho, \quad (10)$$

$$q = -n\chi(\rho)\nabla T = -n\chi\nabla \rho \, dT/d\rho. \quad (11)$$

The $\nabla \rho$ factors represent the poloidal variation on a magnetic flux surface of the 'radial' gradients (in laboratory coordinates) of density and temperatures from one flux surface to the next (see figure 2). The resultant poloidal variation ($\propto |\nabla \rho|$) on the flux surfaces of the electron heat flux from (11) is illustrated in figure 6 at $\rho_N \simeq 0.82$ ($R_{\text{sep}} - R \simeq 6 \text{ cm}$) in 98889. The heat flux is largest on the outboard mid-plane where the magnetic flux surfaces are most closely bunched together (compressed) and the local temperature gradients are largest. The smallest radial heat fluxes occur at the top and bottom (near the LSN divertor X-point) of the tokamak where the flux surfaces are most widely separated and local radial gradients are smallest. In reality, as was explained in the preceding paragraph, the heat fluxes are even more strongly peaked on the outboard mid-plane than is indicated by the Fourier heat flux model in (11) with constant heat diffusivity on a magnetic flux surface that is being used in these codes.

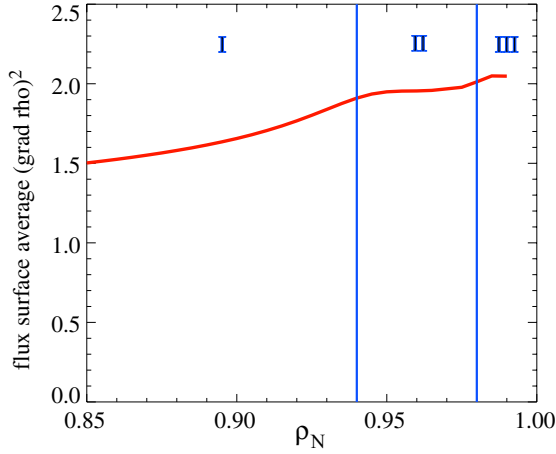


Figure 7. ONETWO radial variation of the dimensionless geometry factor $\langle |\nabla \rho|^2 \rangle$ in the edge.

Substituting the expressions in (10) and (11) into (8) and (9) yields

$$D = \frac{\dot{N}(\rho)}{(dV/d\rho) \langle |\nabla \rho|^2 \rangle (-dn/d\rho)}, \quad (12)$$

$$\chi = \frac{P_{\text{cond}}(\rho)}{(dV/d\rho) \langle |\nabla \rho|^2 \rangle (-n dT/d\rho)}. \quad (13)$$

Using these formulae to determine effective particle and heat diffusivities is usually referred to as interpretive transport modelling. From (3) and the definition of the surface area above (8) we see that the volume factor $dV/d\rho = S(\rho)/\langle |\nabla \rho| \rangle$, in which $S(\rho)$ is the area of the ρ flux surface. For reference, in the pedestal region $0.94 \leq \rho_N \leq 1$, ONETWO indicates $S \simeq 53 \rho_N \text{ m}^2$, $\langle |\nabla \rho| \rangle \simeq 1.22$, and $dV/d\rho \simeq 43.4 \rho_N \text{ m}^2$.

The dimensionless factor $\langle |\nabla \rho|^2 \rangle$ in (12) and (13) is the FSA of the square of the poloidal variation of the heat flux ($\propto |\nabla \rho|$) illustrated in figure 6. It is near unity in the core of tokamak plasmas; for example, in 98889 it is about 1.15 at $\rho_N \simeq 0.5$ (the half-radius of the plasma). Thus, it is often neglected in core transport studies [29]. However, as shown in figure 7, in the pedestal region (II and III) it is of order a factor of 2 and varies modestly with ρ_N there; hence it must be taken into account. For example, the diffusivity values quoted in the ONETWO output files are in fact $\langle |\nabla \rho|^2 \rangle \chi$ and must be divided by $\langle |\nabla \rho|^2 \rangle$ to yield the χ values to be compared with other transport modelling codes and theoretical formulae for $\chi(\rho)$.

The interpretive, effective electron and ion heat diffusivities determined from (13) using the conductive heat flows $P_{\text{cond}} = P_{\text{tot}} - P_{\text{conv}}$ from figure 5 and the $\langle |\nabla \rho|^2 \rangle$ factor from figure 7 are shown in figure 8. Given the wide variety of physics models, coordinate systems and numerical procedures used in the various modelling codes run in their interpretive modes, the degree of agreement between them is satisfactory. Since all the interpretive codes begin from the same plasma profile gradients, differences in these effective diffusivities are primarily due to minor differences in the computed heat flows through various regions of the pedestal. Averaging the interpretive results, the minimum heat diffusivities for

the 98889 pedestal are about $0.3 \text{ m}^2 \text{ s}^{-1}$ for electrons and $0.15 \text{ m}^2 \text{ s}^{-1}$ for ions. The interpretive diffusivities near the minima agree within about 25% for χ_e and 50% for χ_i . The interpretive ion heat diffusivities vary the most mainly because of the differences in the charge-exchange ion heat losses in the pedestal, as indicated in figures 4(b) and 5(b). The different charge-exchange losses result from differences in recycling neutrals fuelling models, which are discussed at the end of section 7. The variations in modelling code results are comparable to the systematic and statistical experimental uncertainties in the gradients obtained from the tanh fits of the n_e and T_e and spline fit T_i profiles (see figure 3) used in these transport analyses.

The strong radial variations of these interpretive, effective heat diffusivities in the pedestal region are generic. The reasons for them can be understood by examining the role of the various terms in (13). As noted above, P_{cond} , V' and $\langle |\nabla \rho|^2 \rangle$ do not vary much in the pedestal region. Thus, variations in the effective heat diffusivities are caused mainly by changes in the magnitudes of the temperature gradients and the density. As ρ_N increases from the core into the pedestal, the effective heat diffusivities first decrease, mainly because the temperature gradients are increasing as ρ_N increases towards and down the top half (II) of the pedestal. The diffusivities reach a minimum a bit before the extrema of the temperature gradients (at symmetry points of the tanh fits at $\rho_N \simeq 0.98$); these minima represent the H-mode pedestal ‘transport barriers’ in electron and ion heat transport. Finally, the interpretive χ values increase in the bottom half (III) of the pedestal as ρ_N increases further outwards towards the separatrix, mainly because the density decreases significantly there; the decreasing magnitudes of the temperature gradients there also contribute slightly.

The specific χ profiles obtained in figure 8 result from the tanh and spline fits to the data used to represent the input data for the modelling codes. However, similar χ_e and χ_i profiles have been obtained from interpretive SOLPS transport modelling of some ASDEX-U H-mode pedestals [30, 31]. Also, GTEDGE modelling of other DIII-D H-mode pedestals [20–23] has obtained similar profiles.

5. Comparisons of heat diffusivities with theoretical predictions

Radial profiles of some theoretically relevant magnetic field structure and plasma transport properties in the edge region are shown in figures 9 and 10. These parameters are obtained from ONETWO modelling using the kinetic EFIT equilibrium flux surfaces in figure 2 and the fitted plasma profiles shown in figure 3. Note that the q profile in figure 9(a) has a slight negative slope in the region $0.955 \lesssim \rho_N \lesssim 0.97$, which causes the global magnetic shear parameter $\hat{s} \equiv (\rho_N/q)(dq/d\rho_N)$ to be negative there. This effect is caused by the increase in the bootstrap current density to about 4.6 times the ohmic current density as ρ_N increases towards the symmetry point of the pedestal ($\rho_{N\text{sym}} \simeq 0.98$).

As figure 9(b) shows, in the pedestal region the gradient scale lengths are small fractions of the average plasma radius a . The pedestal width tanh fit parameter Δ [4, 14, 15] is about twice the normalized gradient scale length at the symmetry

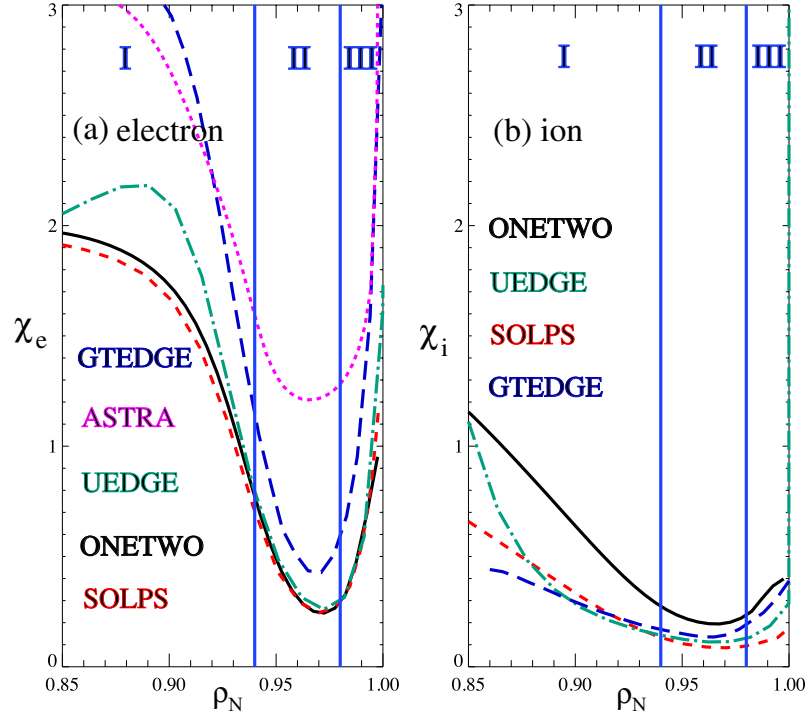


Figure 8. Modelling code results for interpretive, effective diffusivities obtained from (13) for the (a) electron heat diffusivity χ_e ($\text{m}^2 \text{s}^{-1}$) and (b) ion heat diffusivity χ_i ($\text{m}^2 \text{s}^{-1}$).

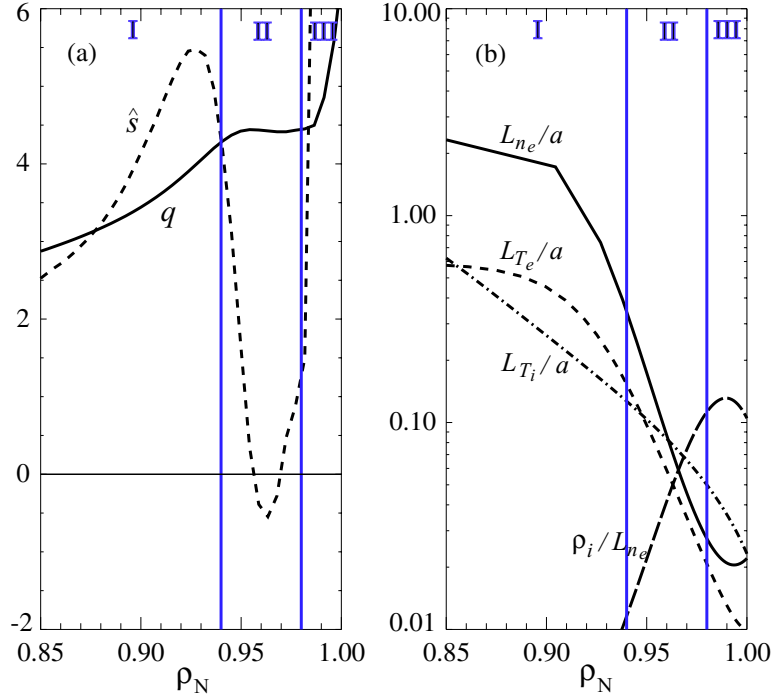


Figure 9. Radial profiles using ONETWO parameters of (a) the ‘safety factor’ q and global magnetic shear parameter $\hat{s} \equiv (\rho_N/q)(dq/d\rho_N)$ and (b) the normalized electron density and electron and ion temperature gradient scale length parameters $L_{n_e}/a \equiv -(\text{d} \ln n_e/\text{d}\rho_N)^{-1}$, $L_{T_e}/a \equiv -(\text{d} \ln T_e/\text{d}\rho_N)^{-1}$ and $L_{T_i}/a \equiv -(\text{d} \ln T_i/\text{d}\rho_N)^{-1}$ in which $a = 0.7667 \text{ m}$. In addition, the ratio of the ion gyroradius $\rho_i \equiv v_{T_i}/\omega_{ci} = \sqrt{2T_i/m_i}/(eB_0/m_i) \sim 0.2 \text{ cm}$ to the electron density gradient scale length L_{n_e} is indicated in the lower right.

point: $\Delta_{n_e} \simeq 0.047 \sim 2 L_{n_e}(\rho_{N\text{sym}})/a$, $\Delta_{T_e} \simeq 0.043 \sim 2 L_{T_e}(\rho_{N\text{sym}})/a$ and $\Delta_{T_i} \simeq 0.106 \sim 2 L_{T_i}(\rho_{N\text{sym}})/a$. Because the ratio of the deuterium ion gyroradius to the density gradient scale length is of order 0.1 or smaller, a small gyroradius

expansion is valid throughout the pedestal. But since the half-width of banana drift orbits are a factor of order $\sqrt{2}q/\sqrt{\epsilon} \simeq 10$ larger than the ion gyroradius in the pedestal region, there could be significant ion orbit losses from the bottom half (III)

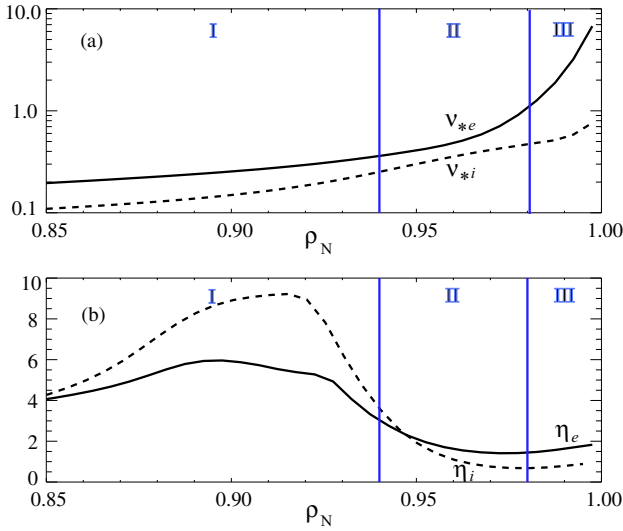


Figure 10. Radial profiles using ONETWO parameters of (a) neoclassical collisionality parameter [32] for electrons (v_{*e}) and ions (v_{*i}) and (b) ratios of gradient scale lengths, $\eta_e \equiv L_{n_e}/L_{T_e}$, $\eta_i \equiv L_{n_i}/L_{T_i}$.

of the pedestal. However, since thermal deuterium ions are near the transition from the banana to plateau collisionality regime there (see figure 10 and the following paragraph), it is likely that only superthermal ions on the tail of the deuterium ion distribution will be lost from this region. Fully ionized carbon ions have smaller gyroradii than deuterium ions by a factor of about $1/\sqrt{6} \simeq 0.4$; they are also more collisional by a factor of $Z_i^2 \simeq 36$. Thus, apparently only ‘high energy tail’ fully stripped carbon ions will contribute to the CER-inferred carbon ion temperatures measured outside the separatrix, as indicated in figure 3(c).

As indicated in figure 10(a), in the core (I) and top half (II) of the edge plasma, thermal electrons and ions are both in the banana collisionality regime ($v_{*s} \ll 1$, $v_{*s} \equiv v_s/(\epsilon^{3/2} v_{Ts}/R_0 q)$, which is $\sqrt{2}$ smaller than the definition in [32]). Fully stripped carbon impurities ($n_C/n_e \simeq 0.061$ in the edge region) are the only significant impurity in DIII-D plasmas. They have been taken into account in the electron and ion collision frequencies via $\nu_e \propto Z_{\text{eff}}$ and $\nu_i \propto [1 + \sqrt{2}(n_e Z_{\text{eff}}/n_i - 1)]/\sqrt{2}$ with $Z_{\text{eff}} \equiv \sum_i n_i Z_i^2/n_e = (n_i + n_C Z_C^2)/n_e \simeq 2.83$ throughout the edge region being considered. Also, $v_{Ts} \equiv (2T_s/m_s)^{1/2}$ and ϵ is an inverse aspect ratio parameter that represents the variation of the magnetic field strength on a flux surface: $\epsilon \equiv (B_{\text{max}} - B_{\text{min}})/(B_{\text{max}} + B_{\text{min}}) \simeq r_M/R_m$, which is $\sim 0.6/1.75 \sim 0.34$ in the pedestal region. Electrons are in the plateau regime ($1 < v_* < \epsilon^{-3/2} \sim 5$) in the bottom half (III) of the pedestal and barely reach the Pfirsch–Schlüter regime ($v_* > \epsilon^{-3/2} \sim 5$) just inside the separatrix (i.e. for $\rho_N > 0.995$). Deuterium thermal ions are near the banana–plateau transition all the way to the separatrix—because T_i does not decrease much in the bottom half (III) of the pedestal.

The parameters $\eta_i (> \eta_{i,\text{crit}} \simeq 1.25$ [33]), $\eta_e (> \eta_{e,\text{crit}} \simeq 1.2$ [34]) and $R_0/L_T = (R_0/a)(a/L_T) \simeq 2.3 (a/L_T) (\gtrsim 10$ for $\rho_N > 0.91$) are all sufficiently large in the core region that ion-temperature-gradient (ITG) and electron-temperature-gradient (ETG) driven drift-wave-type microinstabilities are probable

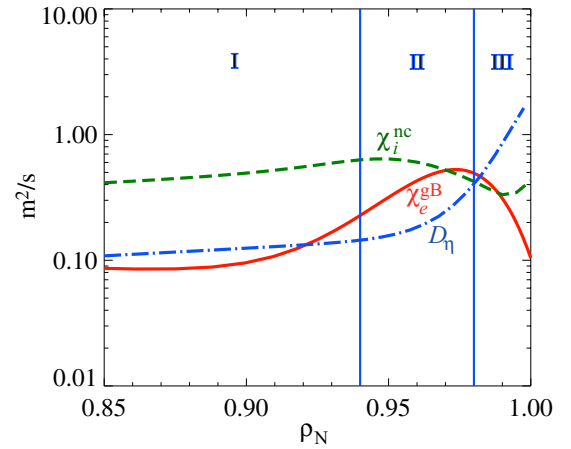


Figure 11. Profiles of characteristic plasma diffusivity coefficients from ONETWO parameters: ETG-induced electron heat diffusion at the electron gyro-Bohm level $\chi_e^{\text{GB}} \equiv (\rho_e/L_{Te})(T_e/eB_{i0}) \simeq 0.075 T_e (\text{keV})^{3/2}/L_{Te} (\text{m}) B_{i0} (\text{T}) \text{ m}^2 \text{ s}^{-1}$, neoclassical ion heat diffusion using the Chang–Hinton formula [39] for χ_i^{nc} , and paleoclassical transport scaled to the magnetic field diffusivity $D_\eta \equiv \eta_{\parallel}^{\text{nc}}/\mu_0 \sim 10^3 Z_{\text{eff}}/[T_e (\text{eV})]^{3/2} \text{ m}^2 \text{ s}^{-1}$.

there. However, ITG modes should be stable in most of the pedestal (II and III) because $\eta_i < 1.25$ there. Dissipative trapped electron modes (TEMs) are likely to be stabilized by the $E \times B$ flow shear [35] in the pedestal region and by the high (plateau) electron collisionality in the bottom half (III) of the pedestal. The shorter wavelength and higher growth rate ETG instabilities are less likely to be stabilized by the flow shear [34]. Finally, the negative global magnetic shear \hat{s} in the region $0.955 \lesssim \rho_N \lesssim 0.97$ can have a stabilizing effect on these drift-wave-type microinstabilities. However, the *local* magnetic shear on the outboard side of divertor plasmas is almost always negative in the pedestal region (II and III) and ETG modes are still unstable there [34].

For a generic scaling perspective on possible plasma transport processes, the radial profiles of some characteristic plasma diffusion coefficients are shown in figure 11. ETG-induced electron heat transport has been advanced [34] as being a significant contributor to electron heat transport in the pedestal; for example, simulation of an ASDEX-U pedestal at a point where $T_e \simeq 0.69 \text{ keV}$ predicted $\chi_e \simeq 0.83 \text{ m}^2 \text{ s}^{-1}$ [34]. In addition, paleoclassical electron heat transport [36, 37] has been advanced as being a major contributor to electron heat diffusion in a different DIII-D pedestal—see figure 14 in [36]. Further, predictive modelling with ASTRA [38] found that for 15 DIII-D H-mode discharges the plasma T_e profiles were best modelled by a combination of electron heat diffusion from ETG-induced anomalous transport near the top of the pedestal (I to II) and paleoclassical transport throughout the pedestal (II and III). Profiles of the underlying characteristic electron gyro-Bohm and magnetic field diffusivities for these two processes are shown in figure 11. From these profiles, we see that ETG-induced transport is a good candidate to dominate near the top of the pedestal (I to II)—because it scales as $T_e^{3/2}$ and T_e is highest there. In the bottom half (III) of the pedestal paleoclassical electron heat transport is a good candidate to dominate—because there the helical multiplier [36] $M < 1$ so it scales as $T_e^{-3/2}$ and T_e is smallest there and decreases as one

moves radially outwards towards the separatrix. Also shown for reference is the predicted neoclassical ion heat diffusivity [32] profile obtained from ONETWO using the Chang–Hinton formula [39].

The magnitude and profile of the sum of the generic predictions for ETG-driven gyro-Bohm level and paleoclassical transport shown in figure 11 are similar to the interpretive effective electron heat diffusivity χ_e shown in figure 8(a). The neoclassical prediction indicated in figure 11 is of the same order of magnitude as the experimentally inferred ion heat diffusivity χ_i shown in figure 8(b); however, its profile is quite different and it is about a factor of 4 larger near the minimum in the interpretive χ_i . Recent calculations with the more precise NEO code [40] have indicated the Chang–Hinton prediction is too large by about 20% in the plasma core; for a typical pedestal the NEO code indicates [41] the true neoclassical χ_i is about 30% smaller than the Chang–Hinton prediction. These calculations include the orbit squeezing effects [42] which are caused by the strong radial variation of the radial electric field in the pedestal. Decreasing the Chang–Hinton prediction by 30%, it still seems that the inferred effective ion heat diffusivity in the 98889 pedestal is *less than* (by a factor ~ 3) the best estimate of the neoclassical ion heat diffusivity there.

The interpretive heat diffusivities have been compared with a wide variety of analytic-based, mixing-length-type theoretical predictions for a number of DIII-D pedestals in [20–23], and most extensively in [43]. For the pedestal in 98889, figures 12 and 13 compare predictions of a number of theoretical models with the interpretive GTEDGE χ_e and χ_i profiles shown in figure 8. Detailed formulae for the various analytic-based theoretical model predictions are given in [43]. To determine radial heat fluxes the GTEDGE interpretive transport model integrates the equilibrium heat transport equations (7) from the separatrix inwards using experimentally determined density and temperature gradients. For this GTEDGE modelling it is assumed that the ratio of ion to electron power flow through the separatrix is 25% to 75%. This is quite close to and between the values of this parameter from ONETWO (28/72) and SOLPS (24/76). The data in figures 12 and 13 are obtained at a slightly different time slice (~ 3962 ms, at the first of the time interval being considered) [23]; however, the profiles and plasma geometry are not significantly different from the profiles shown in figure 3 and the slight differences are not expected to change the conclusions discussed below.

Various points can be made about the theory-experiment electron heat diffusivity comparisons shown in figure 12. As can be seen, the paleoclassical prediction parallels the interpretive, effective $\chi_e(\rho_N)$ in the bottom half of the pedestal (III, $0.98 \leq \rho_N \leq 1.0$) and in the core region (I, $\rho_N \leq 0.94$). There are no points indicated between these regions because integrating as in equations (35) and (36) in [43] from the separatrix region inwards gives negative values for χ_e in this region (II) and the integration outwards from the core becomes inappropriate in this region (II). The four paleoclassical χ_e values in the bottom half (III) of the pedestal, where the paleoclassical helical multiplier $M < 1$, have been estimated in figure 12 by equation (32) in [43].

The spatial variation of the ETG and TEM analytic-based predictions, which include [43] the reductions in growth

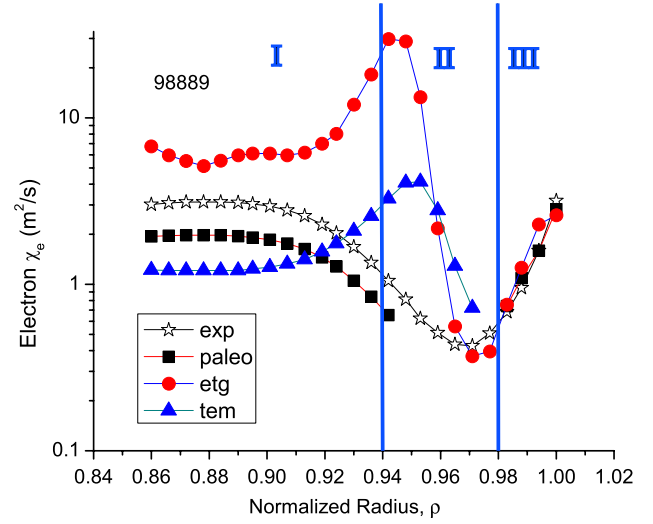


Figure 12. Comparison of interpretive GTEDGE-determined effective electron heat diffusivity χ_e (exp) with analytic-based predictions [43] of various theoretical models: paleoclassical (paleo) collision-induced electron heat transport and electron-temperature gradient (etg) and trapped-electron mode (tem) microturbulence-induced anomalous electron heat transport.

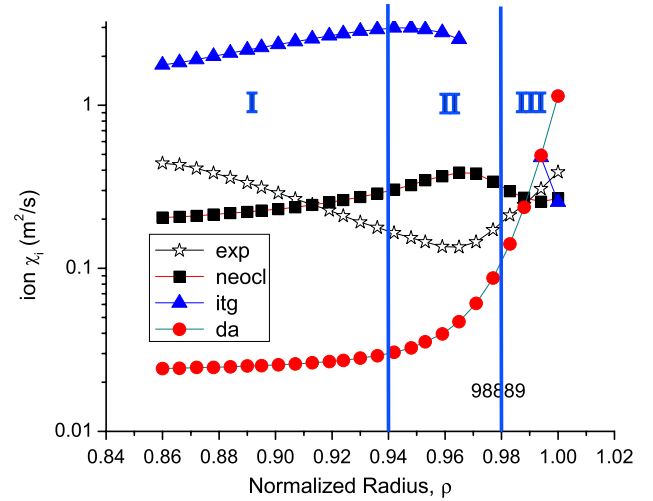


Figure 13. Comparison of GTEDGE-determined effective ion heat diffusivity χ_i (exp) with analytic-based predictions [43] of various theoretical models: neoclassical collision-induced ion heat diffusivity (neocl) and ion-temperature gradient (itg) and drift-Alfvén (da) microturbulence-induced anomalous ion heat transport.

rates caused by $\mathbf{E} \times \mathbf{B}$ flow shear effects, also parallel the interpretive, effective $\chi_e(\rho_N)$ in the core region, but have different magnitudes. In the transition from the core region to the top half of the pedestal they first increase with ρ_N (specifically, for $0.92 \lesssim \rho_N \lesssim 0.95$)—because the analytic-based theoretical formulae in equations (39) and (43) for ETG and TEM transport in [43] are proportional to the magnitude of the ETG which increases with ρ_N there. However, this trend is opposite to the interpretive $\chi_e(\rho_N)$ in this region. The ETG and TEM predictions then decrease rapidly with ρ_N down the top half of the pedestal ($0.95 \lesssim \rho_N \lesssim 0.98$). In the bottom half of the pedestal electrons are in the plateau collisionality regime (i.e. $\nu_{*e} > 1$, see figure 10(a)); hence

TEM modes are stable there. Finally, the ETG χ_e increases with increasing ρ_N in the bottom half of the pedestal primarily because the analytic formula for the ETG-induced transport is inversely proportional to the electron density n_e in this collisional regime. But in the bottom half (III) of the pedestal ETG-induced transport might be limited by the gyro-Bohm scaling factor indicated in figure 11 and hence be negligible there. Direct gyrokinetic simulations (for example, as in [34, 44]) of ETG- and TEM-induced microturbulence, the electron heat transport they induce and the T_e profile they produce are needed to obtain more precise theoretical predictions for these pedestal transport processes.

In summary, none of these electron heat transport models can be unequivocally ruled in or out by this comparison of simple analytic-based theoretical models with the interpretive, effective electron heat diffusivities in this 98889 edge region. However, the paleoclassical model provides perhaps the best overall fit in the pedestal regions where it can be appropriately determined. Also, ETG transport is likely to be a major contributor in the transition from the pedestal (II) into the core (I) region.

Figure 13 shows that for ions the analytic-based theoretical predictions also differ some from the interpretive, effective ion heat diffusivity. As in the discussion of figure 11, the neoclassical ion heat diffusivity is larger than the interpretive χ_i by a factor of about 3 at $\rho_N \sim 0.965$ and has the wrong profile. Here, the neoclassical χ_i has been evaluated using the Chang–Hinton formula [39] specified in equation (1) of [43] using the reduction factor given in equation (6) of [43] to account for orbit squeezing [42].

The ITG transport seems too high in the core region going into the top half (II) of the pedestal; it is not present in the lower parts of the pedestal because the ITG instability criterion in equation (7) of [43] is not satisfied, mainly because $\eta_i < 1.25$ there. However, since the plasma is obviously well above ITG-threshold conditions in the core going into the top half of the pedestal, full gyrokinetic turbulence simulations [44] are needed to clarify the magnitude of the ion heat flux in the core region of this 98889 discharge. Drift-Alfvén microturbulence-induced ion heat transport is apparently negligible in the core but could contribute in the bottom half (III) of the pedestal.

In summary, for ion heat transport, ITG microturbulence-induced transport likely plays a dominant role in the core region (I). Neoclassical transport is likely to be a major contributor in the pedestal region (II and III), where it even seems to be too large by perhaps a factor of 3. However, more detailed gyrokinetic-based simulations will be required to clarify the precise roles and magnitudes of ITG-induced, and perhaps other ion heat pedestal transport processes, including possible ion heat pinch effects.

6. Predictive 1.5D modelling of pedestal electron temperature profile

The preceding transport analyses have focused primarily on interpretive modelling of the 98889 pedestal. In this section for completeness we briefly discuss some ASTRA T_e predictive modelling results [45]. In predictive transport modelling one uses formulae from various analytic-based theoretical models for diffusivities or transport fluxes as input and simulates the

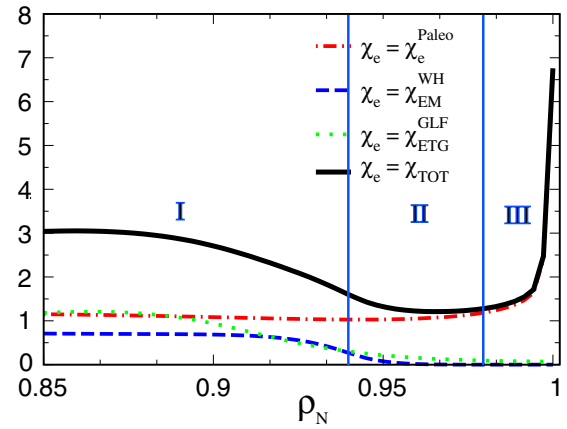


Figure 14. Electron heat diffusivities χ_e ($\text{m}^2 \text{s}^{-1}$) used in ASTRA predictive modelling of the 98889 edge region: paleoclassical [48] χ_e^{Paleo} , Horton [46] electromagnetic ETG $\chi_e^{\text{EM,WH}}$, GLF23 [47] electrostatic ETG $\chi_e^{\text{GLF,ETG}}$ and sum of these three diffusivities χ_{TOT} .

plasma transport evolution to steady state. It seeks to match, within some statistical error, the experimentally obtained quasi-equilibrium plasma profiles.

Previous predictive transport modelling of H-mode plasmas has usually had difficulty modelling the electron temperature profiles—mainly because they did not have a good model of the electron heat diffusivity χ_e in the pedestal. However, recent ASTRA modelling [45] has been quite successful in modelling the overall T_e profiles in 15 DIII-D H-mode discharges. Two aspects of the modelling are critical. First, the density and ion temperature profiles were held fixed; thus, only the electron temperature profile was modelled and evolved to steady state. Second, a wide variety of analytic-based theoretical models were considered and a ‘particular combination of electron thermal transport models’ was developed and applied to all 15 DIII-D H-mode discharges.

The particular electron heat transport model that worked best was composed of ETG-induced and paleoclassical transport models. In particular, the electromagnetic limit of the Horton ETG model [46] was used. In addition, the GLF23 electron heat transport model [47] with the TEM component suppressed (presumably due to $\mathbf{E} \times \mathbf{B}$ flow shear) was used; thus, only GLF23’s electrostatic version of ETG-induced transport is retained. Finally, a paleoclassical electron heat transport model [48] was included.

The contributions of these electron heat transport models to the ASTRA modelling of the 98889 edge region are shown in figure 14 for the 3962 ms time slice. These predictive ASTRA diffusivities are somewhat larger in magnitude but have the same profile as the interpretive results in figure 8(a). These results show that in the core (I) all three models contribute about equally. In the top half (II) of the pedestal ETG transport becomes small and paleoclassical transport begins to become dominant. Finally, in the bottom half (III) of the pedestal the paleoclassical electron heat transport completely dominates.

The electron temperature profile produced by this combination of electron heat transport models is shown in figure 15. The ASTRA-modelled and experimental T_e profiles are in reasonable agreement. However, the ASTRA-modelled electron temperature in the pedestal (i.e. in regions II and III)

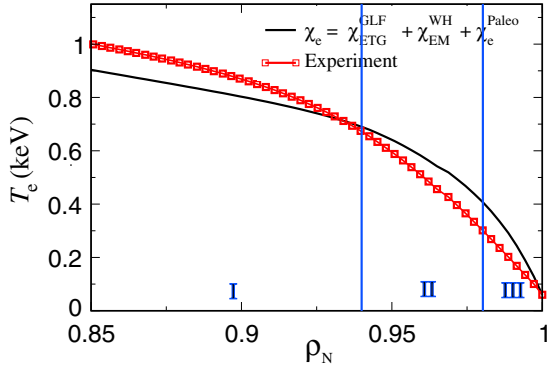


Figure 15. ASTRA predictive T_e modelling results [45] for the combination of electron heat diffusivities shown in figure 14 produces reasonable agreement with the experimentally measured profile in the 98889 edge region.

is somewhat larger than the T_e experimental profile there. In part, this could be the result of only using the lowest order paleoclassical electron heat transport model [48]; heat-pinch-type effects that result from the different structure [49] of the paleoclassical electron heat transport operator could reduce the effective χ_e^{Paleo} in the pedestal region by a factor of 2 or more and thereby increase the magnitude of ∇T_e in the top half of the pedestal.

7. Interpretive 2D modelling

There are two key issues for 1.5D transport modelling in the pedestal region: (1) how far out in radius is it appropriate to use the 1.5D transport model? and (2) what 2D physics effects need to be introduced to extend the transport modelling out to the separatrix ($\rho_N = 1$)? These questions will be addressed in this section with 2D transport modelling, primarily using SOLPS results [50].

These SOLPS 2D transport studies are semi-predictive in that they use the interpretive analysis diffusivities from ONETWO as input and then adjust them slightly in a predictive mode to obtain good agreement with the experimentally measured profiles shown in figure 3. This two-step, semi-predictive procedure provides [50] a very efficient new approach for obtaining transport results with the SOLPS modelling code.

First, we consider the poloidal variation of the electron and ion temperatures on magnetic flux surfaces. Relevant results from SOLPS 2D modelling of the pedestal are shown in figures 16 and 17. For reference, the mapping of ρ_N flux surfaces to $R_{\text{sep}} - R$, which is the radial distance from the separatrix at the vertical elevation of the magnetic axis, is indicated in table 1. As shown in figures 16 and 17, the poloidal temperature variations on flux surfaces throughout the pedestal region are negligibly small (compared with the variation in the magnetic field strength, $\epsilon \sim 0.34$). Even at the outermost surface shown (about 1 mm inside the separatrix, at $\rho_N \simeq 0.997$), the electron and ion temperatures vary by only about 0.13% and 6.5%, respectively. In the SOLPS transport model the ‘source’ that induces these small, approximately sinusoidal poloidal variations in the temperatures is the peaking of the radial heat fluxes on the outboard mid-plane shown in

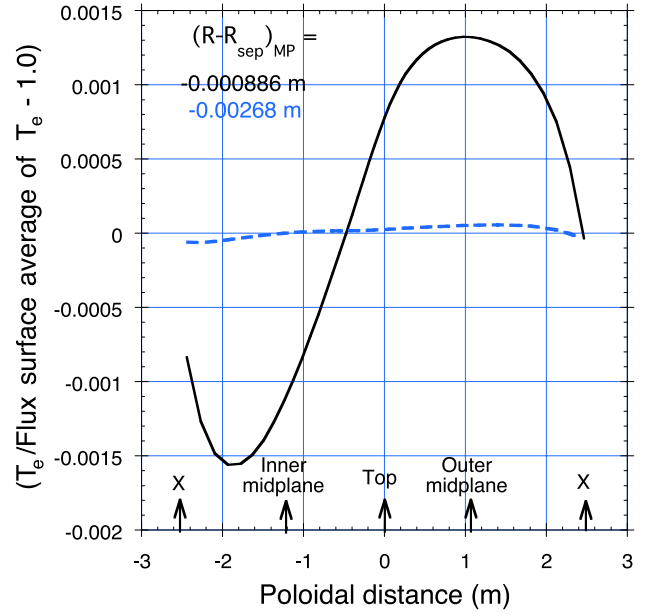


Figure 16. Poloidal variation of electron temperature T_e on pedestal flux surfaces is negligibly small. These results are from SOLPS modelling of 98889 [50].

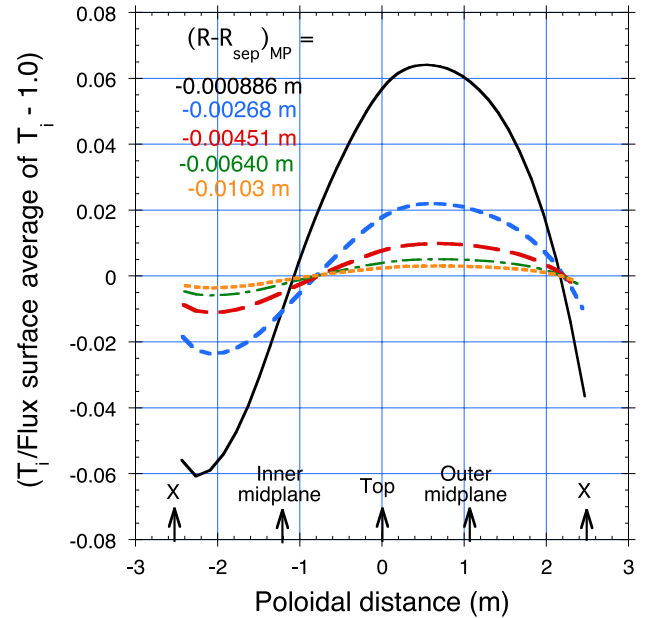


Figure 17. SOLPS poloidal variation of ion temperature T_i on pedestal flux surfaces is negligible except very near the separatrix [50].

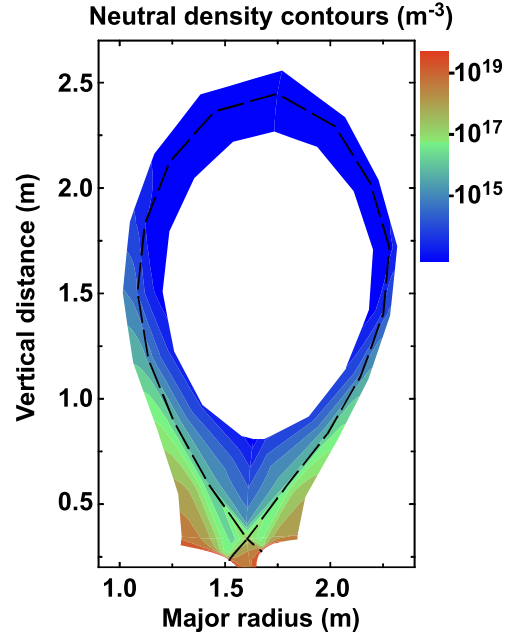
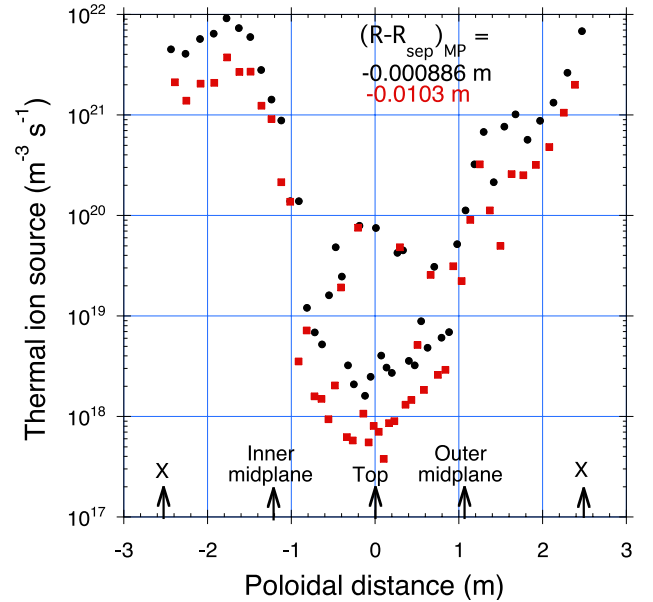
figure 6. The magnitude of the induced poloidal asymmetry is limited by the dissipative relaxation caused by the very large collisional [11] parallel heat conduction. The poloidal variation in the ion temperature is about a factor ~ 50 larger than that in the electron temperature because parallel ion heat conduction is smaller than electron heat conduction by a factor $\sim (m_D/m_e)^{1/2} \sim 60$. Since these temperature variations within flux surfaces are so small, the assumption in the 1.5D modelling codes, which was used in the preceding section, that temperatures are approximately constant on flux surfaces is well justified on all flux surfaces inside the separatrix.

Table 1. Mapping of radial distance (in m and approximate cm) between flux surfaces and the separatrix (on outboard mid-plane) to the normalized radial coordinate ρ_N .

$R - R_{\text{sep}}$ (m)	$R_{\text{sep}} - R$ (cm)	ρ_N
-0.000886	0.09	0.99662
-0.00268	0.27	0.99062
-0.00451	0.45	0.98455
-0.00554	0.55	0.98
-0.00640	0.64	0.97832
-0.01030	1.03	0.96564
-0.01670	1.67	0.94528
-0.0144	1.44	0.95
-0.0175	1.75	0.94
-0.0307	3.07	0.90
-0.0487	4.87	0.85
-0.0682	6.82	0.80

The 2D behaviour of the density is more complicated—because the recycling of thermal neutrals that provides the plasma fuelling in the edge comes predominantly from the poloidally localized X-point region of the LSN divertor separatrix in 98889 (see figure 2 and [50]). A typical contour plot of the 2D neutral density distribution from UEDGE run in an interpretive mode is shown in figure 18. It clearly shows that the neutral density is very strongly peaked near the X-point region. Figure 19 illustrates the Monte-Carlo-based SOLPS modelling of the very large poloidal variation of the deuterium ion source rate S_n just inside the separatrix induced by thermal neutral fuelling from recycling in the divertor region. Since, as shown in figure 2, the 98889 plasma is relatively far from the upper baffles and outboard wall, neutral recycling from the chamber walls has been neglected in this SOLPS modelling [50]. In the pedestal the ion source is a factor of the order of 10^2 smaller at the inboard, outboard mid-planes and top of the flux surface compared with the ion fuelling rate near the X-point. Neutral recycling from the chamber walls could add to the thermal ion source in the top half of the plasma and thereby reduce the asymmetry factor somewhat. However, this should not significantly change the FSA recycling ion source rate obtained from these Monte-Carlo-based SOLPS modelling results, which is shown in figure 22.

The very strong poloidal asymmetries in the recycling neutral density in figure 18 and consequent ion source S_n in figure 19 together with the poloidal variation of the radial particle flux (similar to figure 6) yield the poloidal variations of the electron and deuterium and carbon ion densities shown in figure 20. The poloidal variation in n_e is so small (at most of order 4%, even just inside the separatrix) because of the large electrical conductivity and consequent equilibration of electron density along magnetic field lines. This small electron density variation implies a Boltzmann-type potential variation of $e\delta\Phi/T_e \sim \delta n_e/n_{e0} \sim 0.04$. Electron density and potential variations within flux surfaces of about these magnitudes have been experimentally measured or inferred previously (see figure 6 of [51]) at and just inside the separatrix in DIII-D low power H-mode LSN discharges. The poloidal variation in plasma density in figure 20 is very small and much less than the fractional variation of the magnetic field strength ($\sim \epsilon \sim 0.34$). Thus, the assumption in the 1.5D modelling codes, which was used in the preceding section, that the electron density is approximately constant on flux surfaces

**Figure 18.** 2D neutral density distribution obtained from a typical UEDGE modelling of 98889 shows recycling neutrals are strongly peaked in the LSN X-point region.**Figure 19.** Monte-Carlo-based SOLPS modelling [50] shows that on flux surfaces just inside the separatrix the poloidal distribution of the deuterium ion source produced by neutrals recycling from the divertor are strongly peaked (factor $\sim 10^2$) in the X-point region. The black dots are for the modelling flux surface closest to the separatrix ($R_{\text{sep}} - R \approx 0.1$ cm, $\rho_N \approx 0.997$) and the red boxes are for a flux surface near the top of the pedestal ($R_{\text{sep}} - R \approx 1$ cm, $\rho_N \approx 0.966$).

in the edge plasma is well justified on all flux surfaces inside the separatrix.

The deuterium ion density shown in figure 20 is peaked in the X-point region because the dominant divertor recycling source is strongly peaked there. It is less than its FSA on the outer mid-plane because radial particle flux losses are largest there for the Fick's diffusion law model in (10) used in the

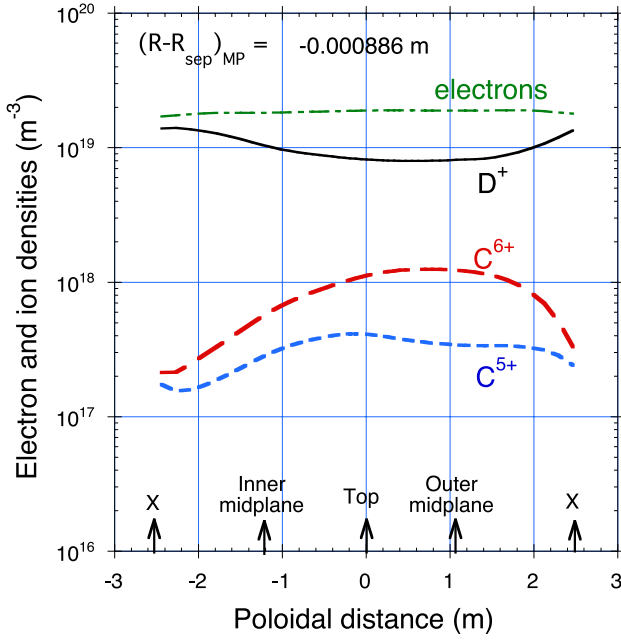


Figure 20. Poloidal variation of the electron density determined from SOLPS modelling [50] is relatively small ($\lesssim 4\%$) on the last modelled flux surface just inside the separatrix ($\rho_N \simeq 0.997$). However, the deuterium and carbon ion densities vary significantly within this near-separatrix flux surface because of the strong deuterium ion source in the X-point region.

SOLPS modelling of this discharge [50]. The carbon densities (of C^{6+} and C^{5+}) are peaked near the outer mid-plane because, as for the electron and ion temperature variations in figures 16 and 17, their primary ‘source’ is provided by radial transport outwards from the core plasma, which is peaked near the outer mid-plane (see figure 6). More details about SOLPS 2D modelling of deuterium and carbon ion densities and flows and their effects on this discharge can be found in [50].

In summary, despite the very large poloidal asymmetry in the recycling neutral density in figure 18 and the consequent ion recycling source shown in figure 19, it appears that on all flux surfaces inside the separatrix the electron density is essentially constant on flux surfaces. And recall that the electron temperature is also essentially constant on flux surfaces in the pedestal. Hence the net particle and electron energy transport in the 98889 pedestal can clearly be described by the 1.5D equations in (6) and (7).

As shown in figure 20, the ion and carbon densities vary poloidally by factors of about two just inside the separatrix in this SOLPS modelling. However, as shown in figure 21, the poloidal variation of the deuterium ion density about its FSA rapidly becomes very small on successive flux surfaces inside the separatrix. In particular, it drops to less than about 15% by the next modelled flux surface at $R_{sep} - R = 0.00268$ m. Thus, except very close to the separatrix (perhaps for $\rho_N > 0.99$, $R_{sep} - R < 2.6$ mm), the deuterium and carbon ion densities can also be assumed to be approximately constant on flux surfaces. Deuterium ion orbit losses in this region could introduce ‘kinetic’ poloidal asymmetry effects near the separatrix. However, presumably only a small fraction of energetic ‘tail’ ions would be on lost orbits because thermal ions in this region (III) are in the transition from the banana to plateau collisionality regime ($\nu_{*i} \gtrsim 0.5$).

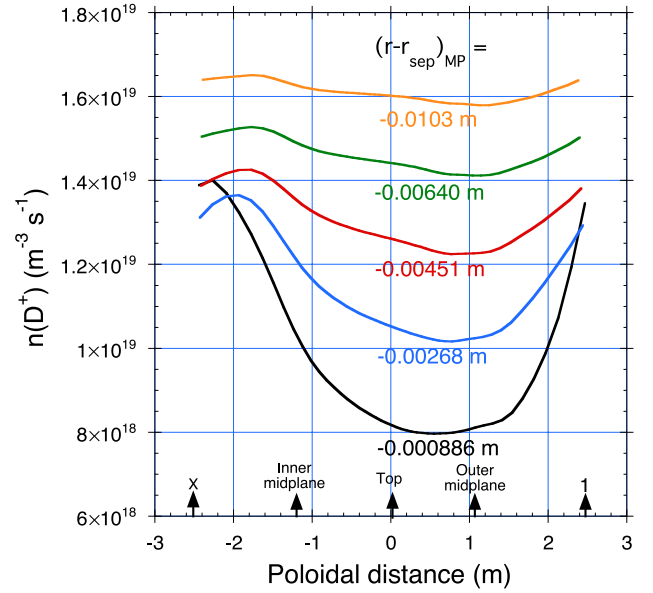


Figure 21. Poloidal variation of the deuterium density from SOLPS modelling [50] shows that it becomes negligible only a short distance from the separatrix.

Hence, the effects of the 2D particle and energy sources will apparently enter transport analyses predominantly through their FSAs, at least out to about $\rho_N > 0.99$. Therefore, within the 1.5D pedestal transport modelling paradigm, the role of the 2D modelling codes is to determine the 2D character of the sources and sinks in the pedestal induced by the 2D effects originating outside the separatrix. Then the FSAs of them are included on the right-hand sides of the transport equations (6) and (7).

The FSA of the modelled recycling ion source is shown in figure 22. This source $\langle S_n \rangle$ is given by the FSA of the product of the neutral density and the $n_e \langle \sigma v \rangle$ collision rate for ionization; i.e. it is proportional to the neutral particle density. The ONETWO results in figure 22 are obtained using a 1D cylindrical model for the recycling neutrals [52] modified to take account of the ‘flux expansion’ effects near the divertor via the Mahdavi model [53]. The 2D SOLPS neutral model is a kinetic Monte-Carlo-based model whose recycling ion source results are shown in figure 19. Its $\langle S_n \rangle$ is larger than the ONETWO value at the separatrix because in SOLPS the diffusion coefficient at the separatrix $D(R_{sep})$ was increased about a factor of 2 to facilitate matching the density profile in the pedestal [50]. Its $\langle S_n \rangle$ is below the ONETWO values for $R_{sep} - R \gtrsim 6.5$ cm ($\rho_N \lesssim 0.8$) because this SOLPS modelling does not include the core neutral beam ionization source whereas ONETWO does. The UEDGE code uses a 2D fluid-based neutral transport model [9]. The GTEDGE code obtains the 2D neutral density distribution from the GTNEUT code [54, 55] which uses an integral transport calculation for the neutral transport based on transmission-escape-probability (TEP) theory. The variability in the recycling plasma source from the divertor region is indicative of the largest uncertainty in the present pedestal transport analyses. More divertor data are needed [50] to reduce these uncertainties.

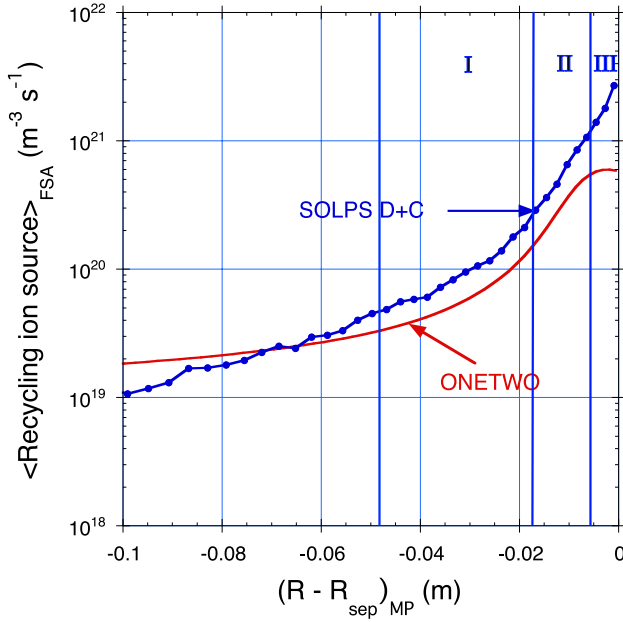


Figure 22. FSA of the recycling source of ions obtained from ONETWO and SOLPS [50] modelling is concentrated near the separatrix.

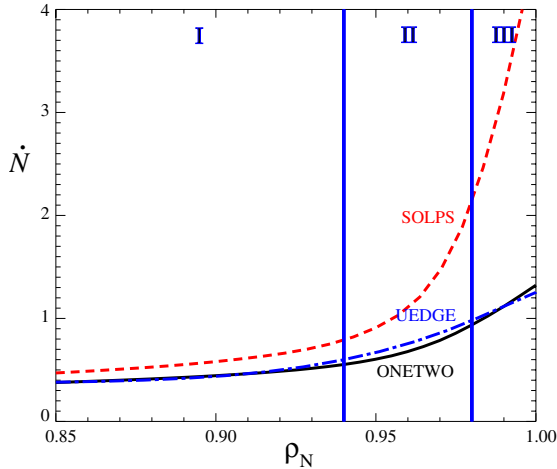


Figure 23. Particle flow rate \dot{N} ($\times 10^{21} \text{ s}^{-1}$) increases with ρ_N in the pedestal region.

8. Density transport

As a first step in exploring density transport, in figure 23 we plot the net flow rate \dot{N} (s^{-1}) defined in (8) of charged particles through flux surfaces as a function of ρ_N . It is obtained from ONETWO, SOLPS and UEDGE modelling of the edge plasma we are considering. In the core region (I) the particle flow rate is approximately constant at $\sim 0.44 \times 10^{21} \text{ s}^{-1}$ or 70 A equivalent. Its near constancy indicates the neutral beam fuelling of the core plasma and its nearly uniform radial transport outwards. The rapid increase in \dot{N} in the pedestal region (II and III) is caused by recycling neutrals providing the edge ion source shown in figure 22. The net increase in outward particle flow \dot{N} over the pedestal of (from ONETWO and UEDGE) $\sim 0.7 \times 10^{21} \text{ s}^{-1}$ ($\sim 110 \text{ A}$ equivalent) is approximately given by $\delta \dot{N} \simeq \langle S_n \rangle$

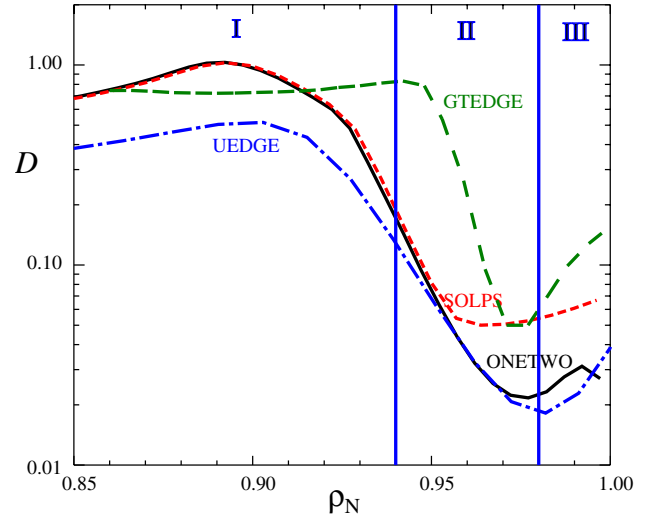


Figure 24. Effective density diffusivity D ($\text{m}^2 \text{ s}^{-1}$) versus ρ_N obtained from GTEDGE, ONETWO, SOLPS and UEDGE interpretive modelling is very small in the pedestal.

$\delta V \simeq (5 \times 10^{20} \text{ m}^{-3} \text{ s}^{-1}) \cdot 1.5 \text{ m}^3 = 0.75 \times 10^{21} \text{ s}^{-1}$. All these modelling codes indicate that the edge recycling fuels the pedestal region (II and III) but is mostly negligible from the top of the pedestal inwards into the core (I).

The interpretive, effective density diffusivity D is obtained by dividing the net particle flow through a flux surface by the density gradient, as defined in (12). The interpretive D profiles obtained this way from the modelling codes are shown in figure 24. There are a number of interesting features of these results. First, it is encouraging that the modelling codes obtain much the same effective density diffusivity profiles, despite significant differences in their analysis procedures and ion source rates, as shown in figures 22 and 23. Next, note that the shapes of the curves are similar to those for effective heat diffusivities in figure 8. Analogous to the reasons for the shapes of the χ profiles, as ρ_N increases outwards from the core (I) and down the top of the pedestal (II), the interpretive D decreases mainly because the magnitude of the density gradient is increasing. Then, after passing the mid-point of the pedestal (III), the effective D increases with increasing ρ_N because of both the increasing particle flow rate \dot{N} and the decreasing magnitude of the density gradient there. It is also noteworthy that the minimum density ‘transport barrier’ value of the effective D is very small. It is about $0.035 \text{ m}^2 \text{ s}^{-1}$ (\pm a factor of almost 2), which is almost an order of magnitude smaller than the effective heat transport barriers in figure 8.

In tokamak plasmas it is often inferred [56] that density transport in the core plasma is not purely diffusive. Instead, the radial density flux seems to be a combination of diffusive outward density transport as in (10) balanced by an inward density pinch flow:

$$\Gamma = -D \nabla n + n V_{\text{pinch}}. \quad (14)$$

Here, V_{pinch} is a negative velocity (m s^{-1}) which indicates an inward ‘pinch’ flow velocity of the species density. Note that V_{pinch} represents radial flow of the species particle distribution as a whole. Thus, it does not necessarily imply that individual particles have an inward ‘pinch velocity’

component; rather, it could just be a fluid moment property of a given plasma species in a tokamak. Alternatively, it could represent: ‘off-diagonal’ transport fluxes (e.g. due to temperature gradients), threshold density gradients (e.g. due to KBMs [26]) beyond which fluctuation-induced transport dramatically increases to produce a form of local ‘profile resiliency,’ or more generally that, as in the paleoclassical density transport model (see equations (74), (75) and (78) in [57]), the density transport operator does not result from a Fick’s diffusion law particle flux as in (10).

There are a number of indications that a strong pinch effect is operative in H-mode pedestals. It was shown in 1993 that ‘flux-surface-averaged transport modelling of the time evolution for the core plasma density profile during H-mode suggests that a strong inward particle pinch is necessary near the separatrix’ [58]. Here, we note that at the top of the pedestal (i.e. at $\rho_N \simeq 0.94$, $R_{\text{sep}} - R \simeq 1.75$ cm) where the density is $\sim 3 \times 10^{19} \text{ m}^{-3}$, the ion source rate from figure 22 is $\langle S_n \rangle \simeq 2 \times 10^{20} \text{ m}^{-3} \text{ s}^{-1}$. Thus, at the top of the pedestal (boundary between I and II) the time scale for all this density to re-build via $\langle S_n \rangle$ after an ELM is $\tau_n \sim n_e / \langle S_n \rangle \sim 150$ ms. However, this time is about an order of magnitude longer than the $\tau_n \sim 10$ ms electron density re-build time observed in the 98889 pedestal (see bottom waveform in figure 1 and discussion of it). The pinch velocity required to re-build the density at the top of the pedestal on this time scale is modest: $V_{\text{pinch}} \sim (1 - \rho_N) a / \tau_n \sim 0.045 \text{ m} / 0.01 \text{ s} \sim 4.5 \text{ m s}^{-1}$. Other indications that pinch effects might be operative in the core plasma just inside the top of the pedestal are (1) the interpretation of ELM-induced transient responses of helium impurities in DIII-D H-mode plasmas imply an inward pinch velocity for them at $\rho_N \sim 0.65$ of about 1 m s^{-1} which increases with ρ_N [59] and (2) the often-observed ‘ears’ [58, 60, 61] on radial profiles of electron density that peak just inside the top of the density pedestal apparently require a pinch-type effect to produce them.

9. Inferring, explaining the density pinch and its consequences

Up to now there has been no way to determine the pinch velocity experimentally, except by analyzing responses to spatially localized transients [56]. However, a recent series of papers [62] have developed an important new interpretive procedure for inferring the pinch velocity. It is based on using [28, 62], in addition to the usual density and energy transport equations, the momentum conservation (force balance) equations. The full procedure [62] includes many terms. In the following we provide a brief description of its main terms and procedural logic. Also, an alternative justification for its proposed representation of key effects on toroidal flow. Thereafter, we present results obtained from this new procedure and compare them with predictions of the paleoclassical density transport model.

The new procedure can be explained in terms of a multiple-time-scale approach [57, 63] to the plasma force balance equations, as follows. On time scales longer than the fast, compressional Alfvén wave time scale ($\sim \mu\text{s}$), the radial force balance yields a (cylindrical-type) relation between the toroidal flow V_ϕ , poloidal flow V_θ and $\mathbf{E} \times \mathbf{B}$ and diamagnetic flows

for the j th species of plasma particles:

$$V_{\phi j} \simeq \frac{E_r}{B_\theta} - \frac{1}{n_j q_j B_\theta} \frac{dp_j}{dr} + \frac{B_\phi}{B_\theta} V_{\theta j}. \quad (15)$$

Here, B_ϕ and B_θ are the magnitudes of the toroidal and poloidal components of the magnetic field. The more general flux coordinate form of (15) is given in equation (8) of [63].

Next the component of the force balance equations along the magnetic field \mathbf{B} is considered [63]; because of the axisymmetry, this is equivalent to the poloidal force balances used in [62]. The parallel/poloidal force balances relax the poloidal flows to their equilibrium values via neoclassical parallel viscous forces [64] on the ion collision time scale, which is of order 1 ms in the pedestal region (II and III). Details of the determination of the equilibrium poloidal flows are given in [62, 63, 65]. The neoclassical-determined poloidal flows in the 98889 pedestal are small contributors to (15) and will mostly be neglected in the following discussion.

Finally, the cylindrical form of the toroidal force balance equation yields a transport time scale equation for the toroidal flow velocity of an ion species j (deuterons or carbon in 98889):

$$m_j n_j \frac{dV_{\phi j}}{dt} = e_j \Gamma_{rj} B_\theta + \sum_k T_{\phi jk} / R + \sum_l M_l. \quad (16)$$

Here, the radial particle flux of the j th species is Γ_{rj} , the sum over k is over the various collisional and microturbulence-induced toroidal torques $T_{\phi jk}$ on the j th ion species, R is the major radius, and the sum over l is over the externally applied momentum inputs M_l (e.g. due to energetic neutral beams), which are negligible in the pedestal. Analogous general flux coordinate forms of the equation for the FSA toroidal rotation frequency $\Omega_t \equiv \mathbf{V} \cdot \nabla \zeta \simeq V_\phi / R$ are given in equation (119) in [57] and equation (22) in [63].

In equilibrium, in the absence of any significant toroidal momentum sources, this last equation yields

$$\Gamma_{rj} = - \sum_k \frac{T_{\phi jk}}{e_j R B_\theta}. \quad (17)$$

This relation shows that the radial particle (density) flux is caused by the sum of the toroidal torques on the plasma species. The seven intrinsically ambipolar particle flux components induced by collisional torques and the eight non-ambipolar particle flux components induced by microturbulence, 3D non-axisymmetric (NA) magnetic field components and other effects are discussed in [57].

The *key representation* used in the new interpretive procedure for determining the radial pinch velocity [62] is that all the toroidal torques (due to charge exchange, microturbulence, 3D field components, etc) on a plasma species j can be written as

$$T_{\phi j}^{\text{an}} / R \equiv -m_j n_j v_{dj} V_{\phi j}. \quad (18)$$

Here, v_{dj} is a ‘drag’ frequency on the toroidal flow caused by the various anomalous plasma transport processes. It is determined [62, 66] from poloidal and toroidal carbon flow experimental data using a combination of the relations in (15) and (16) for the deuteron and carbon species in the edge plasma.

Once the collisional drag frequency ν_{dj} is determined, substituting (18) into (17) and using (15), the radial ion flux of the species j is given by the ‘pinch-diffusion’ relation [62, 66]

$$\Gamma_{rj} \simeq -D_j \left(\frac{1}{T_j} \frac{dp_j}{dr} \right) + n_j V_{rj}^{\text{pinch}}. \quad (19)$$

Neglecting collisional equilibration of ion flows, the density diffusivity and radial pinch velocity are defined by

$$D_j \simeq \frac{m_j T_j \nu_{dj}}{e_j^2 B_\theta^2}, \quad V_{rj}^{\text{pinch}} \simeq \frac{m_j \nu_{dj}}{e_j B_\theta^2} (E_r + V_{\theta j} B_\phi). \quad (20)$$

These formulae are only approximate, illustrative versions of the more comprehensive equations that have been developed [62] and are used for determining these quantities in the 98889 edge plasma [66].

The representation of the toroidal torque $T_{\phi j}^{\text{an}}$ in the drag form given by (18) can also be phenomenologically motivated by first observing [63] that the thermodynamic force $\partial f_{Mj}/\partial r$ for collisional and anomalous radial transport processes can be written as

$$\frac{\partial f_{Mj}}{\partial r} = f_{Mj} \left[\frac{1}{p_j} \frac{dp_j}{dr} + \frac{e_j}{T_j} \frac{d\Phi}{dr} + \left(\frac{\mathcal{E}}{T_j} - \frac{5}{2} \right) \frac{1}{T_j} \frac{dT_j}{dr} \right]. \quad (21)$$

Next, we note that the $|dT_i/dr|$ in the pedestal region (II and III) is typically somewhat weaker than the electron density and temperature gradients there (see figures 3 and 9). Also, for radial transport effects that are not too strongly dependent on the particle energy \mathcal{E} , the $|dT_i/dr|$ term will not contribute significantly when this thermodynamic force is averaged over velocity space. These effects cause the $|dT_i/dr|$ term in (21) to not contribute significantly in the 98889 pedestal (II and III). They also cause the neoclassical-determined poloidal flows in the 98889 pedestal to be small.

Thus, neglecting the poloidal flows in (15) and the $|dT_i/dr|$ term in (21), we see that in the pedestal region

$$\frac{\partial f_{Mj}}{\partial r} \simeq -\frac{e_j B_\theta f_{Mj}}{T_j} V_{\phi j}. \quad (22)$$

Hence, the thermodynamic force for radial plasma transport is roughly proportional to the toroidal flow velocity $V_{\phi j}$ [63]. Then, characterizing diffusive radial transport processes by a microscopic, kinetic diffusion coefficient $(\Delta x)^2/(2\Delta t)$, in which Δx is the random radial step taken in a time Δt (due to 3D NA collisional effects or plasma microturbulence), the radial ion flux can be written phenomenologically as

$$\begin{aligned} \Gamma_{rj} &\simeq -\int d^3v \frac{(\Delta x)^2}{2\Delta t} \frac{\partial f_{Mj}}{\partial r} \simeq D_j \frac{n_j e_j B_\theta}{T_j} V_{\phi j} \\ &\equiv \frac{m_j n_j}{e_j B_\theta} \nu_{dj} V_{\phi j} = -\frac{D_j}{T_j} \left[\frac{dp_j}{dr} - n_j e_j E_r \right]. \end{aligned} \quad (23)$$

The neoclassical toroidal viscosity (NTV) collisional effects of 3D NA toroidal magnetic fields are naturally written in this form when $|dT_i/dr|$ effects are neglected—see equations (106) and (100), (101) in [57]. Microturbulence-induced radial transport of toroidal flow may be diffusive with a coefficient χ_ϕ via the Reynolds stress it induces (see equations (109) and (114) in [57]). Thus, since the thermodynamic force in (22) is proportional to the toroidal flow $V_{\phi j}$, the confinement time for toroidal momentum in the

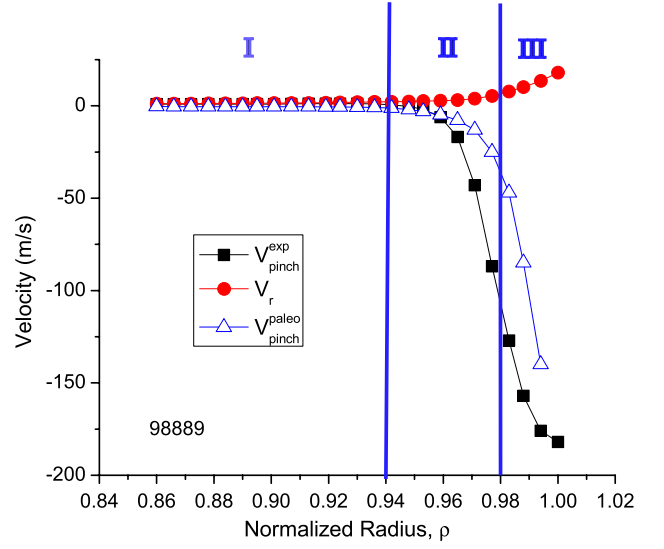


Figure 25. GTEDGE radial flow velocities from: new pinch flow procedure ($V_{\text{pinch}}^{\text{exp}}$, black squares), net (V_r , red circles), and paleoclassical pinch ($V_{\text{pinch}}^{\text{paleo}}$, blue triangles).

pedestal is $\tau_\phi \sim (\delta\rho)^2/\chi_\phi$ in which $\delta\rho$ is the radial width of the pedestal. Therefore, in steady state, microturbulence induces an effective toroidal drag frequency $\nu_{dj} \simeq 1/\tau_\phi \sim \chi_\phi/(\delta\rho)^2$. Both these examples show that forms like the relations in (23) may result from kinetic-based treatments using the thermodynamic force in (22).

Note that the form of the ion flux obtained in (23) is the same as that proposed in (19) for the ion density diffusivity D_j and pinch velocity V_{rj}^{pinch} definitions in (20) when $E_r \gg V_{\theta j} B_\phi$. Thus, when poloidal flows are negligible, consideration of the appropriate thermodynamic force for radial ion transport provides a motivation and possible justification for the new interpretive procedure’s representation of the key effects on the toroidal flow in the drag form stated in (18).

The pinch velocity obtained via the new interpretive procedure for the 98889 edge plasma is shown in figure 25. In the pedestal the inferred ion pinch velocity is inwards and very large—about 100 m s^{-1} at the pedestal mid-point (boundary between regions II and III). Figure 25 also shows that throughout the pedestal region (II and III) the inferred radial pinch velocity is opposite to and about an order of magnitude larger than the interpretive net ion radial ion flow velocity $V_r \equiv \Gamma_{ri}/n_i$. Thus, it seems that the pinch velocity cancels about 90% of the diffusive outward ion flux in the 98889 pedestal in yielding the net radial ion flow velocity V_r . While the density pinch velocity discussed here is the result of an ion-force-balance-based interpretive procedure, it is not a direct experimental measurement of it.

The usual interpretive effective density diffusivity D (i.e. ignoring a pinch) in the pedestal exhibits an apparent very strong transport barrier near the mid-point of the pedestal (i.e. near $\rho_N \sim 0.98$, between regions II and III)—see figures 24 and 26. However, as shown in figure 26, taking account of the very strong pinch flow determined by the new interpretive procedure, the inferred (true?) density diffusivity D_{exp} increases monotonically with ρ_N throughout the pedestal

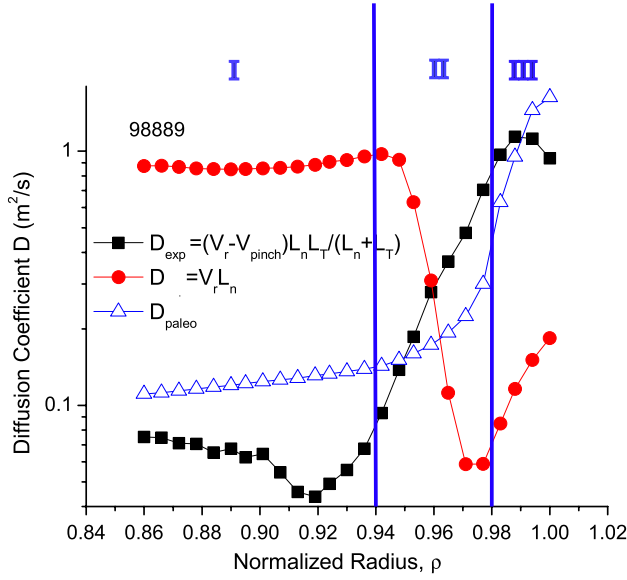


Figure 26. GTEDGE-determined density diffusivities: usual interpretive effective one (D , red circles), inferred (true?) one corrected for inward pinch flow (D_{exp} , black squares) and paleoclassical model (D_{paleo} , blue triangles).

and does not attain a minimum value there. (The D_{exp} value is unusually small in the core region I in this GTEDGE modelling because the ‘pinch flow’ inferred there is outward not inward—because the neutral beam fuelling source has been modeled approximately and perhaps additionally because the poloidal flows become significant there.)

Thus, the very small interpretive effective D near the mid-point of the pedestal may not represent a transport barrier. Rather, it may be an artefact of neglecting the pinch flow in inferring the density diffusivity D . These new pedestal results indicate a diffusively dominant density transport model is likely not appropriate in the pedestal. This has very important and profound implications for the development of a fundamental understanding of radial density transport processes in and fuelling of H-mode pedestals.

Unlike the situation with radial electron and ion heat transport, there are very few analytic-based theoretical models for particle diffusivities, pinch flow velocities and net density transport fluxes, beyond the negligible neoclassical predictions. This is especially true for the plasma parameters in H-mode pedestals. Recently, the paleoclassical transport process [36, 37] has been identified (see discussion after equation (125) in [57]), after the toroidal rotation and hence ambipolar radial electric field are determined and used, as a likely dominant net ambipolar density transport process. As indicated in equations (78) and (125) in [57], the paleoclassical radial density transport flux is

$$\Gamma_r^{\text{paleo}} = -\frac{1}{V'} \frac{\partial}{\partial \rho} (V' \bar{D}_\eta n) = -\bar{D}_\eta \frac{\partial n}{\partial \rho} + n V_{\text{pinch}}^{\text{paleo}}. \quad (24)$$

The paleoclassical density diffusivity \bar{D}_η and pinch flow velocity $V_{\text{pinch}}^{\text{paleo}}$ are

$$\bar{D}_\eta \equiv D_\eta \left\langle \frac{|\nabla \rho|^2 / R^2}{\langle R^{-2} \rangle} \right\rangle, \quad V_{\text{pinch}}^{\text{paleo}} \equiv -\frac{1}{V'} \frac{d}{d\rho} (V' \bar{D}_\eta), \quad (25)$$

in which $D_\eta \equiv \eta_{\parallel}^{\text{nc}} / \mu_0 \sim 10^3 Z_{\text{eff}} / T_e (\text{eV})^{3/2} \text{ m}^2 \text{ s}^{-1}$ is the magnetic field diffusivity induced by the parallel neoclassical resistivity $\eta_{\parallel}^{\text{nc}}$ (see blue dash-dot D_η curve in figure 11) and as above $V' \equiv dV/d\rho$ is the radial derivative of the flux surface volume.

Approximate predictions of the paleoclassical transport model for the density pinch flow and diffusivity are indicated by the blue triangle curves in figures 25 and 26. Here, for simplicity, the radial variations of V' have been neglected and in \bar{D}_η the FSA geometry factor (it is somewhat smaller than the $\langle |\nabla \rho|^2 \rangle$ factor shown in figure 7) has been set to unity; thus, in figure 25 $V_{\text{pinch}}^{\text{paleo}} \simeq -dD_\eta/d\rho$ and in figure 26 $D_{\text{paleo}} \simeq D_\eta$. As can be seen, in the pedestal the paleoclassical predictions are within about a factor of 2 of both the inferred pinch velocity and density diffusivity determined from the new interpretive procedure. Therefore, the paleoclassical transport model provides a plausible explanation of these important new interpretive results.

10. Discussion: what is needed to progress?

The preceding analysis of pedestal transport has highlighted many areas where present modelling is not complete or is inconclusive. In this section we discuss some areas where additional research is needed and some possible new research directions. The various areas discussed in the following paragraphs are heat transport modelling, density transport, new DIII-D pedestals to analyse and pedestals from other tokamaks.

Heat transport modelling. For electron heat transport, the main needs are for detailed gyrokinetic simulations (e.g. as in [34, 44]) of primarily ETG-induced microturbulence throughout H-mode pedestals, and in particular in their bottom halves (III). Also, the complete paleoclassical electron heat transport operator [48, 49] with its heat-pinch-type effects needs to be taken into account. For ions, a number of areas need to be examined in greater detail: precise neoclassical ion heat diffusivity calculations (e.g. as in [40]), kinetic calculations including the effects of electric-field-induced orbit squeezing and ion orbit losses, ITG-induced microturbulence simulations and consideration of possible paleoclassical ion heat diffusivity and pinch effects. Also, for KBMs [26] precise instability criteria, fluctuation spectra and their nonlinear and transport consequences need to be explored.

Density modelling. This is a crucial area that needs considerably more attention. The general need here is for more recent DIII-D H-mode discharges in which more density-related quantities are measured, particularly in the divertor region. Divertor region measurements are needed to pin down the neutral density and recycling ion source in this region to facilitate a more precise determination of the ‘pedestal boundary conditions’ for these quantities and the radial density transport in the vicinity of the separatrix. Also, direct experimental measurements of density pinches via analysis of transient responses (after L–H transition, ELMs) are needed to experimentally validate the new strongly coupled density pinch-diffusion model discussed in section 9. In addition, much more consideration and modelling, including of the dynamics, of density transport with strong pinch effects is

needed. Further, the degree of importance of 2D effects may be able to be explored by determining the poloidal variation of the carbon density just inside the separatrix (see figure 20). Finally, poloidal and toroidal plasma flows in the vicinity of the separatrix need to be explored [50] to determine the possible roles and importance of such effects in pedestal plasma transport.

New DIII-D pedestals to analyse. In general, more pedestals from DIII-D need to be analysed to see how universal the pedestal transport properties identified in this paper are. Particularly useful would be pedestals with the following characteristics: (1) better diagnosed pedestals with more divertor region data; (2) pedestals with higher and lower collisionality; (3) wider pedestals with more spatial resolution, particularly in the bottom half of pedestal and (4) microturbulence fluctuation data throughout the pedestal looking in particular for intermittent bursts of fluctuations (e.g. due to KBMs [26]) just before ELMs that could presage their occurrence or cause ‘profile resiliency.’ Finally, studies of paired DIII-D discharges with opposite grad-B drift directions would be useful for exploring flows and their effects both outside and just inside the separatrix.

Pedestals from other tokamaks. Of course the ultimate test of one’s understanding is that it also applies to other tokamak plasmas. Thus, it is desirable to analyse H-mode pedestals from other tokamaks with a focus on well-diagnosed pedestals with long transport quasi-equilibria after an L–H transition and between ELMs, and the widest possible range of machine and dimensionless parameters.

11. Summary

Plasma transport in one DIII-D pedestal (98889) was modelled with many transport modelling codes: 1.5D interpretive (ONETWO, GTEDGE), 1.5D predictive (ASTRA) and 2D (SOLPS, UEDGE) ones. The general conclusions from this multi-faceted study are (1) magnetic flux surface geometry effects ($q \propto \nabla\rho$, $(|\nabla\rho|^2)$ factor) are important in the pedestal; (2) the modelling codes generally agree on effective diffusivities if proper comparisons are made; (3) the 1.5D transport models are apparently appropriate for $\rho_N \lesssim 0.99$ using the flux-surface-averaged 2D sources and sinks, with the caveat that kinetic effects due to ion orbit losses from the bottom half of the pedestal could modify this fluid-model-based conclusion for the ions and (4) the largest uncertainties are in the magnitudes of the recycling thermal neutral density and ion source coming from the divertor X-point region, which influence ion heat and density transport.

Tentative conclusions about plasma transport in the 98889 DIII-D H-mode pedestal are (1) ‘transport barrier’ interpretive, effective diffusivities are small: 0.3 (*e* heat), 0.15 (*i* heat), 0.035 (*n*) $\text{m}^2 \text{s}^{-1}$; (2) generic scalings and interpretive and predictive transport modelling all indicate that electron heat transport is likely dominated by ETG effects at the pedestal top (I to II transition) plus paleoclassical transport throughout the edge plasma region (I, II and III); (3) the less well quantified ion heat transport is likely ITG-induced at the pedestal top (I and transition into II) with a significant neoclassical component in

the pedestal (II and III) that may be too large in region II and has the wrong profile there and (4) density transport may be determined, using a new interpretive procedure, by a strong pinch flow that nearly cancels the outward diffusive density flux, which indicates that the usually inferred deep density transport barrier may be an artefact of neglecting the pinch, and the inferred V_{pinch} and D_{exp} are approximately given by the predictions of the paleoclassical density transport model. While there are strong modelling, interpretative analysis and paleoclassical model predictions for a strong density pinch in the pedestal, it should be emphasized that there is as yet no direct experimental measurement of the density pinch and/or its effects.

This study has identified (in section 10) the following needs for reaching more definitive conclusions about plasma transport in H-mode pedestals: (1) divertor data to better determine the flux-surface-average ion source from the divertor region and the resultant radial density transport on the separatrix; (2) microturbulence simulations and neoclassical calculations for the entire pedestal region; (3) much greater attention to density transport in the pedestal including plausible strong pinch flow effects and (4) analysis of other DIII-D H-mode pedestals and pedestals from other tokamaks.

Acknowledgments

This paper was prepared for presentation at the 12th International Workshop on ‘H-mode Physics and Transport Barriers,’ 30 September–2 October 2009, Princeton Plasma Physics Laboratory, Princeton, New Jersey. The authors are grateful to R.E. Waltz for drawing our attention to the fact that the usual ONETWO output files for the interpretive heat diffusivities give $\langle |\nabla\rho|^2 \rangle \chi$, not χ . This research was supported by US DoE grants and contracts DE-FG02-92ER54139 (UW), DE-FC02-04ER54698 (GA), DE-AC05-00OR22725 (ORNL), DE-FG02-92ER54141 (Lehigh), DE-AC52-07NA27344 (LLNL), DE-FG02-00ER54538 (GaTech).

Appendix A. Coordinate systems used in 1.5D and 2D modelling codes

To specify the divergences of particle and energy fluxes in (1) and (2), we need to specify a coordinate system. Because the various codes use different coordinate systems, we will utilize a generic coordinate system that encompasses all of them. The coordinates of a general curvilinear coordinate system are usually identified as $u^i \equiv (u^1, u^2, u^3)$. Because of the toroidal axisymmetry, the third coordinate will always be taken to be the toroidal angle: $u^3 \equiv \zeta = \phi$. Since we are mainly interested in ‘radial’ transport across flux surfaces, it is convenient to choose the radial coordinate to be a flux surface label. To be general we use $u^1 \equiv x_\psi$, in which x_ψ is ρ , ρ_N , Ψ_N or $R - R_{\text{sep}}$ on the horizontal mid-plane. Finally, a poloidal angle variable is needed. For it we use $u^2 \equiv x_\theta$, in which x_θ is a poloidal angle θ or a poloidal distance ℓ (x in 2D codes) along a flux surface. The Jacobian of the transformation from laboratory (x) to the (possibly nonorthogonal) u^i curvilinear coordinates is $\sqrt{g} \equiv 1/\nabla u^1 \cdot \nabla u^2 \times \nabla u^3 = (d\psi_p/dx_\psi)/B \cdot \nabla x_\theta$.

The specific coordinates used in the various transport modelling codes are

ONETWO: $x_\psi \rightarrow \rho \equiv \sqrt{\Phi/\pi B_{t0}}$ (m), $x_\theta \rightarrow \ell$ (m),
 $\sqrt{g} = 1/B \cdot \nabla \ell \equiv 1/B_p(\rho, \ell)$.
 ASTRA: $x_\psi \rightarrow \rho \equiv \sqrt{\Phi/\pi B_{t0}}$ (m), $x_\theta \rightarrow \theta$ (radians),
 $\sqrt{g} = 1/B \cdot \nabla \theta \equiv \rho/B_{pol}(\rho, \theta)$.
 GTEDGE: $x_\psi \rightarrow \bar{r}$ (m), $x_\theta \rightarrow \theta$ (geometric angle,
 radians), $\sqrt{g} \equiv H = 1/B \cdot \nabla \ell_\theta$.
 SOLPS, UEDGE: $x_\psi \rightarrow y$ (m), $x_\theta \rightarrow x$ (m), $\nabla x_\psi =$
 \hat{e}_y/h_y , $\nabla x_\theta = \hat{e}_x/h_x$, $\sqrt{g} = h_x h_y R$.

In the ONETWO and ASTRA codes the flux surfaces are determined from the EFIT Grad-Shafranov solver [13]. The GTEDGE code uses [28, 67] the analytic Miller equilibrium [27] model of the EFIT flux surfaces to calculate the poloidal ($x_\theta \rightarrow \theta$) dependence of ∇T and ∇n (see section 4); it calculates heat and particle fluxes in an equivalent circular cross-section geometry model that conserves flux surface area in the elliptical approximation, which yields $\bar{r} = r[(1 + \kappa^2)/2]^{1/2}$ in which κ is the vertical elongation of flux surfaces.

In the 1.5D modelling codes (ONETWO, ASTRA, GTEDGE) the radial and poloidal angle coordinates used in developing them are not orthogonal, i.e. $\nabla x_\psi \cdot \nabla x_\theta \neq 0$ —because of the toroidal geometry. The nonorthogonal coordinates can be chosen such that, on a flux surface, the magnetic field lines are straight (i.e. $\zeta = q(\psi)\theta + \zeta_0$); this is a very useful property for analytic analyses in these low collisionality plasmas where the collision length λ exceeds the poloidal periodicity length $2\pi R_0 q$. However, on a magnetic separatrix all the 1.5D code coordinate systems become invalid because at the X-point $B \cdot \nabla x_\theta$ vanishes and the Jacobian is undefined ($\sqrt{g} = 1/B \cdot \nabla x_\theta \rightarrow \infty$). Thus, these 1.5D code coordinate systems can only be used inside a separatrix.

In the 2D codes (SOLPS, UEDGE) the flux surfaces are taken to be the EFIT equilibrium flux surfaces, which are labelled locally by $x_\psi \rightarrow y$. The poloidal coordinate $x_\theta \rightarrow x$ is defined as being locally orthogonal to the local radial flux surface coordinate. Thus, the 2D x, y and $R\zeta \rightarrow z$ coordinates represent locally Cartesian coordinates. (It is important to note that this choice of local coordinates is unfortunately the opposite of that used in the vast plasma instability literature where x is usually a radial coordinate and y is a poloidal-type coordinate.) In SOLPS and UEDGE the metric factor $h_\zeta \equiv 1/|\nabla \zeta|$ for the toroidal direction is taken to be $2\pi R$; but for consistency of notation here, we take $\nabla \zeta = \hat{e}_\zeta/h_\zeta$ with $h_\zeta = R$ (in m) and integrate over ζ to obtain the 2π factor. In the SOLPS, UEDGE formulae above $\hat{e}_x, \hat{e}_y, \hat{e}_\zeta$ are unit vectors in the x, y, ζ directions, respectively. These orthogonal 2D code coordinates are applicable both inside and outside the separatrix and are very useful in the collisional regime outside the separatrix. However, they are not as useful in the hot core plasma because magnetic field lines are not straight in them (i.e. $\zeta = \int_0^x dx' (d\zeta/dx')_{x'} + \zeta_0 = \int_0^x dx' (B \cdot \nabla \zeta / B \cdot \nabla x)_{x'} + \zeta_0 = f(x, y) + \zeta_0$), which makes analytic calculations more difficult with them.

Since for a general curvilinear coordinate system the divergence of a vector \mathbf{A} is $\nabla \cdot \mathbf{A} = \sum_i (1/\sqrt{g})(\partial/\partial u^i)(\sqrt{g} \mathbf{A} \cdot \nabla u^i)$ and because of axisymmetry $\partial/\partial \zeta = 0$, we obtain for $\mathbf{A} = \Gamma \equiv n\mathbf{V}$ [or $\mathbf{A} \equiv \mathbf{q} + (5/2)T\Gamma$]

$$\nabla \cdot \Gamma = \frac{1}{\sqrt{g}} \frac{\partial}{\partial x_\theta} (\sqrt{g} \Gamma \cdot \nabla x_\theta) + \frac{1}{\sqrt{g}} \frac{\partial}{\partial x_\psi} (\sqrt{g} \Gamma \cdot \nabla x_\psi), \quad (\text{A.1})$$

$$\sqrt{g} = \nabla x_\psi \cdot \nabla x_\theta \times \nabla \zeta, \quad \text{Jacobian.} \quad (\text{A.2})$$

Thus, the density and energy equations can be written in the generic coordinates as

$$\frac{\partial n}{\partial t} + \frac{1}{\sqrt{g}} \frac{\partial}{\partial x_\theta} (\sqrt{g} \Gamma \cdot \nabla x_\theta) + \frac{1}{\sqrt{g}} \frac{\partial}{\partial x_\psi} (\sqrt{g} \Gamma \cdot \nabla x_\psi) = S_n, \quad (\text{A.3})$$

$$\begin{aligned} \frac{\partial}{\partial t} \left(\frac{3}{2} nT \right) + \frac{1}{\sqrt{g}} \frac{\partial}{\partial x_\theta} \left(\sqrt{g} \left(\mathbf{q} + \frac{5}{2} T \Gamma \right) \cdot \nabla x_\theta \right) \\ + \frac{1}{\sqrt{g}} \frac{\partial}{\partial x_\psi} \left(\sqrt{g} \left(\mathbf{q} + \frac{5}{2} T \Gamma \right) \cdot \nabla x_\psi \right) = Q. \end{aligned} \quad (\text{A.4})$$

These are the equations solved in the 2D modelling codes SOLPS and UEDGE.

In the 2D codes the parallel (to the magnetic field \mathbf{B}) conductive electron and ion heat fluxes are assumed to be given by the classical, collisional Braginskii [11] formulae. The projection of the dominant parallel conductive heat flow in the generic poloidal direction is $\mathbf{q} \cdot \nabla x_\theta = -(\mathbf{B} \cdot \nabla x_\theta / B)^2 n \chi_\parallel \partial T / \partial x_\theta$, in which χ_\parallel is the classical collisional parallel heat diffusivity. In section 7 we discuss the 2D code solutions of (A.4); they show that for the pedestal we are considering the very large parallel electron and ion heat diffusivities $\chi_{e\parallel}$ and $\chi_{i\parallel}$ cause the electron and ion temperatures to become nearly constant along magnetic field lines and hence on flux surfaces throughout the pedestal region. In addition, in the 2D codes the electron parallel collisional friction relaxes the electron density along field lines. Thus, for the present transport analyses the most important plasma transport processes in the pedestal region will be those that transport particles and heat radially across magnetic flux surfaces.

References

- [1] Kinsey J.E., Bateman G., Onjun T., Kritiz A.H., Pankin A., Staebler G.M. and Waltz R.E. 2003 *Nucl. Fusion* **43** 1845
- [2] Aymar R., Chuyanov V.A., Huguet M., Shimomura Y., ITER Joint Central Team and ITER Home Teams 2001 *Nucl. Fusion* **41** 1301
- [3] Luxon J. 2002 *Nucl. Fusion* **42** 614
- [4] Groebner R.J., Osborne T.H., Leonard A.W. and Fenstermacher M.E. 2009 *Nucl. Fusion* **49** 045013
- [5] St John H.E., Taylor T.S., Lin-Liu Y.-R. and Turnbull A.D. 1995 *Proc. 15th IAEA Fusion Energy Conf. on Plasma Physics and Controlled Nuclear Fusion Research (Seville, 1994)* (Vienna: International Atomic Energy Agency) vol 3 p 60
- [6] Stacey W.M. 1998 *Phys. Plasmas* **5** 1015; **8** 3673 (2001); *Nucl. Fusion* **40** 965 (2000)
- [7] Pereverzev G. and Yushmanov P.N. 2002 ASTRA automated system for transport analysis in a tokamak *Technical Report IPP 5/98*, Max-Planck Institut für Plasmaphysik
- [8] Schneider R., Bonnin X., Borrass K., Coster D.P., Kastelewicz H., Reiter D., Rozhansky V.A. and Braams B.J. 2006 *Contrib. Plasma Phys.* **46** 3
- [9] Rognlien T.D., Rensink M.E. and Smith G.R. 2007 *User Manual for the UEDGE Edge-Plasma Transport Code Lawrence Livermore National Laboratory Report UCRL-ID-137121*, 28 January 2000 (Updated 23 February 23 2007)
- [10] Rognlien T.D. and Rensink M.E. 2002 *Fusion Eng. Des.* **60** 497
- [11] Braginskii S.I. 1965 *Rev. Plasma Phys.* ed M.A. Leontovich (New York: Consultants Bureau) vol I p 205

- [12] Zeng L., Wang G., Doyle E.J., Rhodes T.L., Peebles W.A. and Peng Q. 2006 *Nucl. Fusion* **46** S677
- [13] Lao L.L. *et al* 1990 *Nucl. Fusion* **30** 1035
- [14] Porter G.D., Moller J., Brown M., Lasnier C. and the DIII-D Team 1998 *Phys. Plasmas* **5** 1410
- [15] Groebner R.J. *et al* 2001 *Nucl. Fusion* **41** 1789
- [16] Osborne T.H., Snyder P.B., Burrell K.H., Evans T.E., Fenstermacher M.E., Leonard A.W., Moyer R.A., Schaffer M.J. and West W.P. 2008 *J. Phys.: Conf. Ser.* **123** 012014
- [17] Martin Y. and ITPA threshold database working group 2008 *J. Phys.: Conf. Ser.* **123** 012033
- [18] Carlstrom T.N. *et al* 1992 *Rev. Sci. Instrum.* **63** 4901
- [19] Gohil P., Burrell K.H., Groebner R.J., Kim J., Martin W.C., McKee E.L. and Seraydarian R.P. 1991 *Proc. 14th Symp. in Fusion Engineering (San Diego, CA)* vol 2 (New York: Institute of Electrical and Electronics Engineers) p 1199
- [20] Stacey W.M. and Groebner R.J. 2006 *Phys. Plasmas* **13** 072510
- [21] Stacey W.M. and Evans T.E. 2006 *Phys. Plasmas* **13** 112506
- [22] Stacey W.M. and Groebner R.J. 2007 *Phys. Plasmas* **14** 012501
- [23] Stacey W.M. and Groebner R.J. 2007 *Phys. Plasmas* **14** 122504
- [24] Hirshman S.P. and Jardin S.C. 1979 *Phys. Fluids* **22** 731
- [25] Terry P.W. *et al* 2008 *Phys. Plasmas* **15** 062503
- [26] Snyder P.B., Groebner R.J., Leonard A.W., Osborne T.H. and Wilson H.R. 2009 *Phys. Plasmas* **16** 056118
- [27] Miller R.L., Chu M.S., Greene J.M., Lin-Liu Y.R. and Waltz R.E. 1998 *Phys. Plasmas* **5** 973
- [28] Stacey W.M. 2008 *Phys. Plasmas* **15** 122505
- [29] Waltz R.E. and Miller R.L. 1999 *Phys. Plasmas* **6** 4265
- [30] Horton L.D. *et al* 2005 *Nucl. Fusion* **45** 856
- [31] Chankin A.V. *et al* 2006 *Plasma Phys. Control. Fusion* **48** 839
- [32] Hinton F.L. and Hazeltine R.D. 1976 *Rev. Mod. Phys.* **48** 239
- [33] Jenko F., Dorland W. and Hammett G.W. 2001 *Phys. Plasmas* **8** 4096
- [34] Jenko F., Told D., Xanthopoulos P., Merz F. and Horton L.D. 2009 *Phys. Plasmas* **16** 055901
- [35] Waltz R.E., Kerbal G.D. and Milovich J. 1994 *Phys. Plasmas* **1** 2229
- [36] Callen J.D. *et al* 2007 *Nucl. Fusion* **47** 1449
- [37] For derivations of the paleoclassical key hypothesis see J.D. Callen 2007 *Phys. Plasmas* **14** 040701; **14** 104702 (2007); **15** 014702 (2008)
- [38] Rafiq T., Pankin A.Y., Bateman G., Kritz A.H. and Halpern F.D. 2009 *Phys. Plasmas* **16** 032505
- [39] Chang C.S. and Hinton F.L. 1982 *Phys. Fluids* **25** 1493
- [40] Belli E.A. and Candy J. 2008 *Plasma Phys. Control. Fusion* **50** 095010
- [41] Belli E.A. 2010 private communication
- [42] Shaing K.C. and Hazeltine R.D. 1992 *Phys. Fluids B* **4** 2547
- [43] Stacey W.M. 2008 *Phys. Plasmas* **15** 052503
- [44] Candy J., Holland C., Waltz R.E., Fahey M.R. and Belli E. 2009 *Phys. Plasmas* **16** 060704
- [45] Rafiq T., Pankin A.Y., Bateman G., Kritz A.H. and Halpern F.D. 2009 *Phys. Plasmas* **16** 032505
- [46] Horton W. *et al* 1988 *Phys. Fluids* **31** 2971
- [47] Waltz R.E. *et al* 1997 *Phys. Plasmas* **4** 2482
- [48] Callen J.D. 2005 *Nucl. Fusion* **45** 1120
- [49] Callen J.D. 2005 *Phys. Plasmas* **12** 092512
- [50] Owen L.W., Canik J.M., Groebner R.J., Callen J.D., Bonnin X. and Osborne T.H. 2010 *Nucl. Fusion* **50** 064017
- [51] Schaffer M.J., Bray B.D., Boedo J.A., Carlstrom T.N., Colchin R.J., Hsieh C.-L., Moyer R.A., Porter G.D., Rognlien T.D., Watkins J.G. and the DIII-D team 2001 *Phys. Plasmas* **8** 2118
- [52] Burrell K.H. 1978 *J. Comput. Phys.* **27** 88
- [53] Mahdavi M.A., Maingi R., Groebner R.J., Leonard A.W., Osborne T.H. and Porter G. 2003 *Phys. Plasmas* **10** 3984
- [54] Stacey W.M. and Mandrekas J. 1994 *Nucl. Fusion* **34** 1385
- [55] Zhang D.-K., Mandrekas J. and Stacey W.M. 2006 *Phys. Plasmas* **13** 062509
- [56] Gentle K.W. *et al* 1992 *Phys. Rev. Lett.* **68** 2444
- [57] Callen J.D., Cole A.J. and Hegna C.C. 2009 *Phys. Plasmas* **16** 082504
- [58] Rensink M.E., Allen S.L., Futch A.H., Hill D.N., Porter G.D. and Mahdavi M.A. 1993 *Phys. Fluids B* **5** 2165
- [59] Wade M.R. *et al* 1995 *Phys. Plasmas* **2** 2357; *J. Nucl. Mater.* **220–222** 178 (1995)
- [60] Sykes A. *et al* 2001 *Phys. Plasmas* **8** 2101
- [61] Maingi R. *et al* 2002 *Phys. Rev. Lett.* **88** 035003
- [62] Stacey W.M. 2004 *Phys. Plasmas* **11** 4295; *Contrib. Plasma Phys.* **48** 94 (2008). Stacey W.M. and Groebner R.J. 2005 *Phys. Plasmas* **12** 042504; **15** 012503 (2008)
- [63] Callen J.D., Cole A.J. and Hegna C.C. 2009 *Nucl. Fusion* **49** 085021
- [64] Hirshman S.P. and Sigmar D.J. 1981 *Nucl. Fusion* **21** 1079
- [65] Houlberg W.A., Shaing K.C., Hirshman S.P. and Zarnstorff M.C. 1997 *Phys. Plasmas* **4** 3230
- [66] Stacey W.M. and Groebner R.J. 2009 *Phys. Plasmas* **16** 102504
- [67] Stacey W.M. and Bae C. 2009 *Phys. Plasmas* **16** 082501